ALMA MATER STUDIORUM
UNIVERSITÀ DI BOLOGNA

DEPARTMENT OF INDUSTRIAL ENGINEERING

SECOND CYCLE DEGREE IN
MECHANICAL ENGINEERING FOR SUSTAINABILITY

……

CFD SIMULATION AND EXPERIMENTAL VALIDATION OF INFLOW/OUTFLOW STRUCTURE SERVING RETROFITTED PUMPED STORAGE HYDROPOWER PLANT

Dissertation in ICAR/01: EXPERIMENTAL FLUID MECHANICS

Supervisor	**Defended by**
Prof. Massimo Guerrero	**Roshan Singh**

Graduation Session: March 24, 2026

Academic Year 2024/2025

Acknowledgements

I would like to express my deepest gratitude to Prof. Massimo Guerrero, whose guidance, expertise, and constant encouragement have been fundamental throughout the development of this thesis. His clarity of vision and commitment to scientific rigor have shaped both this work and my growth as a researcher. Also his attention to the finest details and dedication have played a major role in shaping the pathway for this work and future collaborations as well.

My sincere thanks go to Rezar Lleshi, whose support as a PhD collaborator has been invaluable. His willingness to perform experimentation,discuss ideas, troubleshoot challenges, and share his experience made this journey far more insightful and rewarding.

I am also grateful to Alberto Boninsegni for his essential contribution in preparing the experimental setups and ensuring that all laboratory requirements were met. His technical skill and dedication were crucial to the successful execution of the experimental campaign.

Finally, I extend my appreciation to the Hydraulic Engineering Laboratory (LIDR) at the Department of Civil, Chemical, Environmental and Materials Engineering (DICAM), University of Bologna. The facilities, resources, and collaborative environment provided an exceptional setting in which to carry out this research.

Contents

1 Introduction

As the energy landscape of the world is being heavily focused on carbon neutrality, transitioning to renewable energy sources has become the focal point for most of the energy production industries. The European Union particularly is committed to becoming the world's first climate-neutral continent by 2050, with a legally binding target to reduce net greenhouse gas emissions by at least 55% by 2030 and to achieve a minimum 42.5% share of renewable sources in its energy mix by the same year [10]. However, the increased trend of relying on Solar Thermal and Wind Energy, and other technologies such as TESS(Thermal Energy Storage Systems) presents significant challenges for grid stability and energy security. Pumped storage hydropower (PSH) systems are re-establishing themselves as front runners for carbon-neutral energy transition. As a mature and large-scale form of energy storage, PSH systems are flexible to store excess energy generated during off-peak periods as hydraulic pressure energy , converting it back to electric power during peak demand which effectively balances the supply and demand of energy over time [1]. Recent findings have predicted that without sufficient long-term storage like PSH, the EU faces potential risks of not properly utilizing its renewable energy capacity and compromising its climate targets [8]. Thus, the development and retrofitting of PSH plants is essential to align the energy sector with the EU's broader vision for a sustainable, net zero-carbon future.

PSH systems have been used to generate power from turbining operations between the higher reservoir and the lower reservoir during peak hours of load requirements and then use the same power to pump water from the lower reservoir to the higher reservoir , storing potential energy during low load requirements or off-peak hours. Since reservoirs are connected to rivers upstream and downstream that supply them with sediments, sediment dynamics in reservoirs is a very important phenomenon that must be carefully investigated for proper functioning of power generation activities as well as to ensure the longevity of the reservoir and mechanical components [2].

In order to comprehend the sediment transport phenomenon in reservoirs, various methodologies have been successfully applied. The most common are using numerical models and scaled physical models. Numerical models allow researchers to develop the optimal 3-d design of the reservoir and the intake/outlet structure or to replicate the design of an existing reservoir, and to choose optimal hydrodynamic and sediment transport parameters. This numerical model can then be validated with the help of a scaled physical model using experimental techniques involving the use of Particle Image Velocimetry(PIV),Acoustic Doppler Velocimeter (ADV) , etc. to measure the velocity fields and sediment concentrations. Bermúdez et al. [4] developed 3-d numerical simulations and a scaled physical model to provide guidance in the application of hydraulic modeling procedures to locate and design intake-outlet structures in existing lakes or reservoirs.This can be useful during the planning stages of power plants to aim for the shortest possible waterways between the reservoirs while ensuring adequate flow conditions.Similarly,Hosseini et al. [14] used acoustic back-scattering analysis techniques using ADV in a physical model to estimate sediment concentration in turbidity currents close to the bed, where it is difficult to obtain reliable concentration data using sampling techniques.

To understand the sediment deposition, suspension, advection and scouring/erosion caused by flushing waves , Campisano et al. [7] developed experimental and numerical models using a rectangular laboratory channel and a mobile bed. The numerical model is based on the semi-coupled solution of the complete De Saint Venant equations for the water flow and of the Exner equation for the sediment continuity. The sediment scouring process is particularly important in narrow channels because it can deposit significant amounts of sediments at the bottom of the reservoir where fluid velocities are relatively low compared to the channel. This is a disadvantage for the long term operation of the reservoirs since it reduces the storage capacity and causes the obstruction of intakes and the abrasion of hydraulic machinery[5]. In such a case, flushing waves and venting of turbidity currents are useful phenomena to restore the health of reservoirs.Chamoun et al. [9] performed an extensive review of venting turbidity currents process and concluded that it can become a means to prolong a reservoir's life when applied in an optimal way.

To evaluate the erosion and deposition dynamics of fine suspended sediments, Yang et al. [34] performed an analysis of six field campaigns carried out during dam flushing events in the Arc- Isère river system in the Northern French Alps. Suspended sediment flux (SSF) and discharges were analysed and the variations between two or more measurement locations were attributed to change in the hydrology and morphology of the rivers and also due to natural flooding events. This analysis highlights the sediment dynamics in rivers, which has to be taken into account for the overall dynamics in the reservoirs.

The aim of this study is to assist the design of inflow/outflow structures of the PSH systems, where turbulent flows are dominant and play a vital role in the scouring and sediment transport process .To achieve this , the turbulent flow was implemented using various approaches while modelling the channel of the PSH system. The Reynolds-Averaged Navier Stokes(RANS) turbulence model is particularly useful in reproducing mean flow features along with shear stresses in the near-wall regions and boundary layers.This model is useful to supplement the sediment transport behaviour since the shear stress is the major contributor to scouring and bed load movement of the sediment layer. Another turbulence model that is consistently used in hydraulics is Large Eddy Simulation(LES). LES is efficient in reproducing the rotating vortex structures and eddies. The turbulent eddy sizes range from large eddies of the size of the flow domain corresponding to low frequency fluctuations, to small eddies corresponding to high frequency fluctuations at which viscous forces act and dissipation takes place [24].The large eddies break into small eddies dissipating their energy , the process is called energy cascading. The LES model is particularly important to emulate the dynamic behaviour of sediment entrainment, suspension, resuspension as well as advection. So, in order to understand which turbulence model can efficiently replicate the turbulent flow and sediment transport behaviour, specific case of flow in the reservoir of the PSH system was simulated and evaluated using both turbulence models and validated with the data obtained from experimentation.

2 Objective and Tasks

The primary objective of this study is to develop a robust numerical model for simulating the hydrodynamic and sedimentation processes associated with pumped-storage hydropower (PSH) operations capable for both turbining and pumping phases, and to validate the developed numerical model with a scaled experimental model. This approach is particularly valuable in scenarios where PSH systems are implemented using existing reservoirs, as it enhances project cost-efficiency and helps mitigate environmental impacts [6]. Special attention is given to analyzing near-field flow dynamics at the intake/outlet structures and within the connecting channel.

The primary objective can be further developed into the following set of tasks:

- Construction of the numerical domain
- Implementation of the Turbulence model. Two different turbulence models are used for separate sets of simulations:
  - RANS (RNG k-ε) Model
  - LES Model
- Implementation of the Sediment Transport model
- Comparison of the two turbulence models in terms of velocity fields and sediment dynamics
- Construction of a scaled Physical/Experimental model
- Validation of the two numerical models with the data from experiments using the physical model
  - Validation of velocity fields
  - Validation of Sedimentation process

3 Numerical Model

The numerical model was primarily developed using Flow-3D Hydro, the commercial CFD (Computational Fluid Dynamics) software by Flow Science Incorporated, used for simulating hydraulics and sediment transport cases.The versions of the Flow-3D software adopted was 2025R1. The advantage of this software over other commercial software is that it includes features for free surface modelling with Tru-VOF method, where two or more fluids are used , specifying their volume fraction at each boundary. For example, at free surface the volume fraction of water should be specified as zero while that of air as 1 approximately. Also, the package includes a wide range of features to simulate diverse physical models such as Variable Density Flow, Air Entrainment, Sediment Transport, Dispersed Multiphase Flow ,Cavitation, Tailings, Wind, Granular flow, Scalars and Particles, etc. A detailed description of these models can be found at [12].

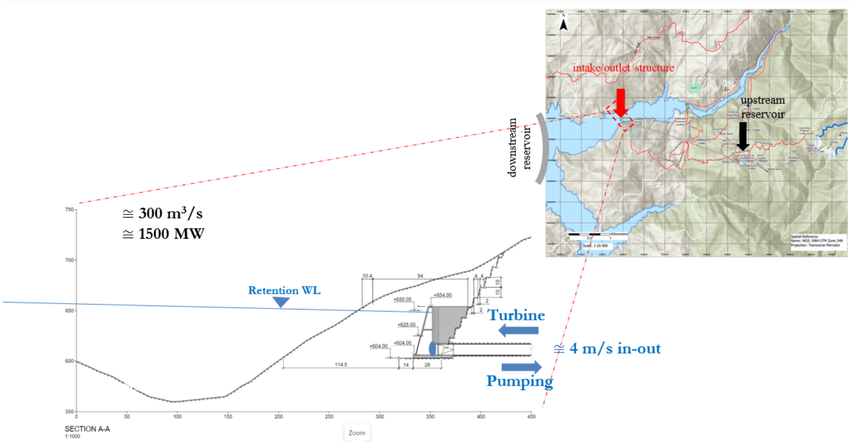

Figure 1: Bathymetry and Initial Plan for the Lower Reservoir

The 3D-modelling for the computational domain of lower reservoir for the PSH system was performed in SolidWorks and a STL(Stereolithography) file was imported. The 3D-model comprises of the pipe intake/outlet structure with a diameter of 9.80 m , which opens into a channel, following which is the larger and wider reservoir/lake with a downward slope, the plateau section and then an upward slope(Fig. 1) .Figure 2 provides detailed views of the numerical model with dimensions, focusing on the intake/outlet structure along with the narrow channel.

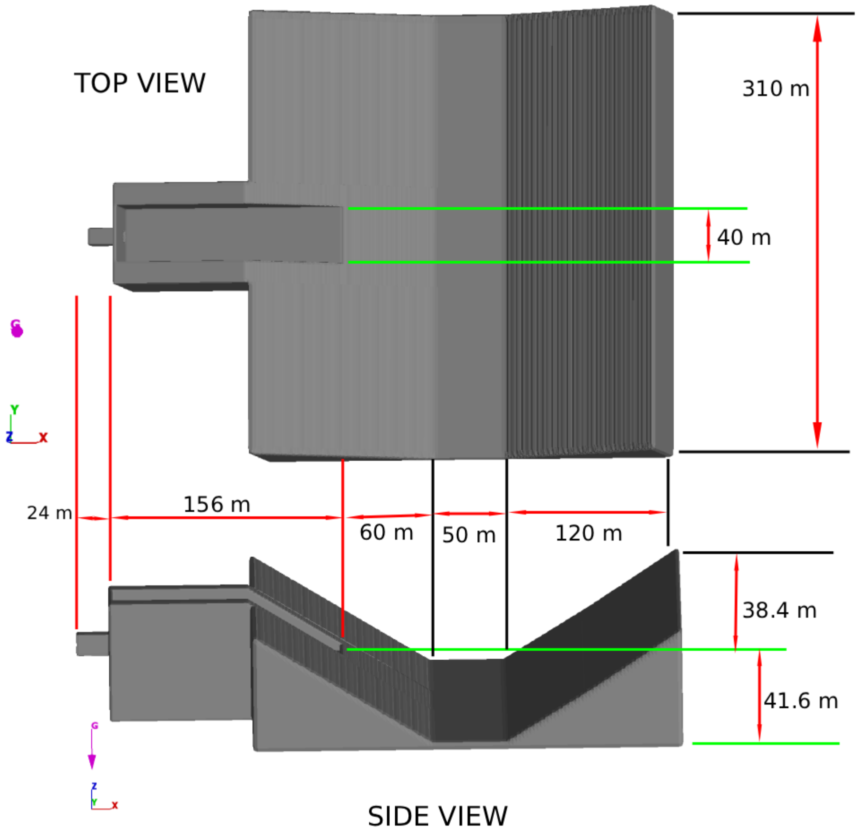

(a) Side and Top View with Dimensions

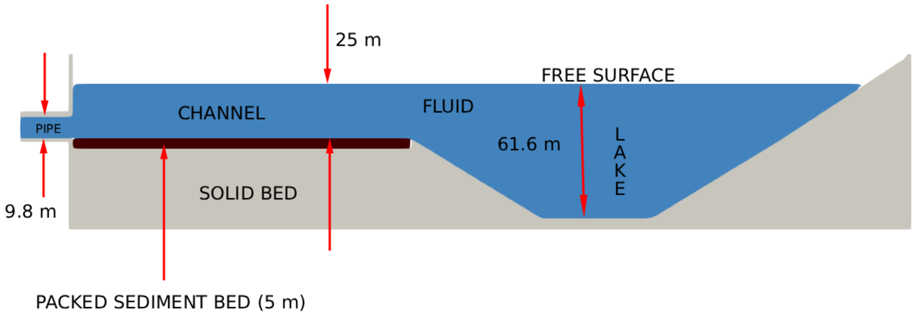

(b) Sectional View with regions and water levels

Figure 2: Numerical Domain of lower reservoir model with intake/outlet pipe and narrow channel

This computational domain was then imported into the FLOW-3D HYDRO software. The physical models chosen for the initial simulations were : Gravity and non-inertial, Viscosity and turbulence. Gravity was specified in the negative Z-direction, meaning a constant hydrostatic pressure with a certain water level.This is consistent with the hydraulic condition resulting in the Froude number($Fr = \mathrm{U}/\sqrt{gH}$) equal to 0.26 , indicating sub-critical, gravity-dominated flow, where the free surface remains stable and turbulence is primarily governed by shear rather than inertial instabilities.Since the outflow/inflow for the turbining/pumping operations lies in the turbulent region, the RNG(ReNormalization Group) k-ε and Large Eddy Simulation(LES) models were used for the simulations.The k-ε and LES models have been shown to provide reasonable approximations to many types of flows [26].

3.1 Turbulence Model

3.1.1 RNG k-ε Model

For the aforementioned k-ε model, two transport equations are solved , one for the turbulent kinetic energy k_T and the other for turbulent dissipation rate ε_T.The transport equation for the turbulent kinetic energy k_T is(Equation 1):

$$\frac{\partial k_T}{\partial t} + \frac{1}{V_F}\left\{uA_x\frac{\partial k_T}{\partial x} + vA_y\frac{\partial k_T}{\partial y} + wA_z\frac{\partial k_T}{\partial z}\right\} = P_T + G_T + \mathrm{Diff}_{k_T} - \varepsilon_T \tag{1}$$

where V_F, A_x, A_y, and A_z are FLOW-3D HYDRO's FAVOR functions, and P_T represents the turbulent kinetic energy production term which is given by(Equation 2):

$$\begin{aligned} P_T = \text{CSPRO} \cdot \frac{\mu}{\rho V_F} \cdot \Bigg[\\ 2A_x \left(\frac{\partial u}{\partial x}\right)^2 + 2A_y \left(R\frac{\partial v}{\partial y} + \xi\frac{u}{x}\right)^2 + 2A_z \left(\frac{\partial w}{\partial z}\right)^2 + \\ \left(\frac{\partial v}{\partial x} + R\frac{\partial u}{\partial y} - \xi\frac{v}{x}\right) \cdot \left(A_x\frac{\partial v}{\partial x} + A_y\left(R\frac{\partial u}{\partial y} - \xi\frac{v}{x}\right)\right) + \\ \left(\frac{\partial u}{\partial z} + \frac{\partial w}{\partial x}\right) \cdot \left(A_z\frac{\partial u}{\partial z} + A_x\frac{\partial w}{\partial x}\right) + \\ \left(\frac{\partial v}{\partial z} + R\frac{\partial w}{\partial y}\right)\left(A_z\frac{\partial v}{\partial z} + A_y R\frac{\partial w}{\partial y}\right)\Bigg] \end{aligned} \tag{2}$$

where CSPRO is a turbulence parameter with default value of 1.The buoyancy production term G_T is (Equation 3):

$$G_T = -\text{CRHO}\left(\frac{\mu}{\rho^2}\right)\left(\frac{\partial \rho}{\partial x}\frac{\partial p}{\partial x} + R^2\frac{\partial \rho}{\partial y}\frac{\partial p}{\partial y} + \frac{\partial \rho}{\partial z}\frac{\partial p}{\partial z}\right) \tag{3}$$

where μ is the molecular dynamic viscosity, ρ is the fluid density, p is the pressure, CRHO is another turbulence parameter, whose default value is 0.0, but for thermally buoyant flow problems should be chosen to be approximately 2.5. The diffusion term Diff_{k_T} is given by(Equation 4):

$$\text{Diff}_{k_T} = \frac{1}{V_F}\left(\frac{\partial}{\partial x}\left(\nu_k A_x \frac{\partial k_T}{\partial x}\right) + R\frac{\partial}{\partial y}\left(\nu_k A_y R\frac{\partial k_T}{\partial y}\right) + \frac{\partial}{\partial z}\left(\nu_k A_z\frac{\partial k_T}{\partial z}\right) + \xi\frac{\nu_k A_x k_T}{x}\right) \tag{4}$$

where ν_k is the diffusion coefficient of k_T and is computed based on the local value of the turbulent viscosity. Similarly , the transport equation for turbulent dissipation rate is as follows:

$$\frac{\partial \varepsilon_T}{\partial t} + \frac{1}{V_F}\Big(uA_x\frac{\partial \varepsilon_T}{\partial x} + vA_yR\frac{\partial \varepsilon_T}{\partial y} + wA_z\frac{\partial \varepsilon_T}{\partial z}\Big) = \frac{\mathrm{CDIS1}\cdot\varepsilon_T}{k_T} \Big(P_T + \mathrm{CDIS3}\cdot G_T + \mathrm{Diff}_\varepsilon - \mathrm{CDIS2}\cdot\frac{\varepsilon_T^2}{k_T}\Big) \tag{5}$$

where CDIS1, CDIS2, and CDIS3 are all dimensionless user-adjustable parameters, and have defaults of 1.44, 1.92 and 0.2, respectively for the k-ε model.This equation reduces the need for a user-specified value of turbulent length TLEN throughout the domain, which is necessary to be specified in the one-equation models.

The diffusion of dissipation is given by (Equation 6):

$$\mathrm{Diff}_\varepsilon = \frac{1}{V_F}\left(\frac{\partial}{\partial x}\left(\nu_\varepsilon A_x\frac{\partial \varepsilon_T}{\partial x}\right) + R\frac{\partial}{\partial y}\left(\nu_\varepsilon A_y\frac{\partial \varepsilon_T}{\partial y}\right) + \frac{\partial}{\partial z}\left(\nu_\varepsilon A_z\frac{\partial \varepsilon_T}{\partial z}\right) + \xi\frac{\nu_\varepsilon A_x\varepsilon_T}{x}\right) \tag{6}$$

where ν_ε is the diffusion coefficient of ε_T .

The RNG turbulence model builds upon the foundational structure of the standard k-ε model but derives its constants analytically through statistical techniques rather than relying on empirical calibration [33]. This theoretical rigor enhances its predictive capabilities, particularly in flows characterized by high strain rates, streamline curvature, and low turbulence intensity [3]. Compared to the standard formulation, the RNG model has demonstrated superior performance in capturing complex flow features such as recirculation zones and shear layers [21]. In our CFD simulations of the reservoir, the RNG model was specifically chosen to better resolve strong shear zones near the intake and outlet structures, where accurate representation of turbulence dissipation and velocity gradients is critical for assessing sediment transport and hydraulic behaviour. Prior studies have also shown that RNG-based models outperform their linear counterparts in compressible and anisotropic flow regimes, further validating its applicability to our domain [21].

The RNG model uses equations similar to those of the k-ε model.The equation constants that are found empirically in the k-ε model are derived explicitly in the RNG model. The default values of RMTKE , CDIS1 and CNU used are 1.39 , 1.42 and 0.085 respectively, whereas CDIS2 is computed from k_T and P_T terms.The turbulent kinematic viscosity is computed as(Equation 7) :

$$\nu_T = \mathrm{CNU}\frac{k_T^2}{\varepsilon_T} \tag{7}$$

A numerical challenge that persists in both the k-ε and the RNG model is to limit the value of ε_T . The transport equation for turbulent diffusion may produce values of ε_T close to zero, and in order to cope with that the values of k_T should also approach zero, but does not do so. So, the values of ν_T become very high as can be observed from 7 . So , the value of ε_T should be limited to a minimum value given by(Equation 8)

$$\varepsilon_{\mathrm{T,min}} = \mathrm{CNU}^{\frac{3}{4}}\frac{k_T^{\frac{3}{2}}}{\mathrm{TLEN}} \tag{8}$$

where TLEN is the maximum turbulent length scale, which can be defined by the user or limited automatically.

3.1.2 Large Eddy Simulation Model

The Large Eddy Simulation (LES) model computes the larger energy-containing turbulent structures than can be resolved by the defined computational grid , while modeling and approximating only the smaller, subgrid-scale (SGS) structures. The idea and need of LES originated from atmospheric turbulence modeling and is three-dimensional and time-dependent. It requires as a pre-requisite the introduction of turbulent fluctuations/oscillations as the inflow boundary condition and sufficiently fine spatial resolution to capture the larger eddies [28]. Compared to Reynolds-averaged approaches, LES provides richer information on unsteady flow structures, coherent vortices, and temporal variability, although at a higher computational cost.

In LES, the Navier–Stokes equations are spatially filtered, obtaining transport equations for the filtered velocity field $\bar{u}_i$. This filtering operation introduces the Sub-Grid

Scale(SGS) stress tensor given by(Equation 9)

$$\tau_{ij}^{\mathrm{SGS}} = \overline{u_i u_j} - \bar{u}_i \bar{u}_j \tag{9}$$

This SGS tensor represents the effect of the unresolved fluctuations on the resolved motion, which need to be modelled by a subgrid-scale model [25]. FLOW-3D employs an eddy-viscosity SGS model based on the classical Smagorinsky model [28], in which the anisotropic(deviatoric) part of the SGS stress is related to the resolved strain-rate tensor(Equation 11):

$$\tau_{ij} = -2\nu_T \bar{S}_{ij} \tag{10}$$

$$\tau_{ij}^{\mathrm{SGS}} - \frac{1}{3}\tau_{kk}^{\mathrm{SGS}}\delta_{ij} = \tau_{ij} \tag{11}$$

where the isotropic part of the SGS stress tensor includes the sum of the normal stresses τ_{kk}^{SGS} , which is double the kinetic energy of the SGS fluctuations and acts like pressure.Similarly the resolved strain-rate tensor is given by(Equation 12)

$$\bar{S}_{ij} = \frac{1}{2}\left(\frac{\partial \bar{u}_i}{\partial x_j} + \frac{\partial \bar{u}_j}{\partial x_i}\right) \tag{12}$$

The SGS eddy viscosity ν_T is computed as(Equation 13)

$$\nu_T = (C_s\, L)^2 \sqrt{2\bar{S}_{ij}\bar{S}_{ij}} \tag{13}$$

where C_s is the Smagorinsky coefficient, typically in the range 0.1–0.2, and L is the filter length scale. In FLOW-3D, the filter length scale is defined as the geometric mean of the local grid spacing(Equation 14):

$$L = (\delta x\, \delta y\, \delta z)^{1/3}. \tag{14}$$

This SGS eddy viscosity is added to the dynamic viscosity and used throughout the momentum equations in the same manner as for the turbulence transport models. This formulation provides the dissipation of energy from the smallest resolved scales to the larger unresolved scales within the inertial subrange.

Despite the extensive applicability of the Smagorinsky model for its robustness and simplicity, several refinements have made to the SGS eddy viscosity model in the broader LES literature to better predict the sub-grid stresses.The dynamic procedure computes the coefficient C_s by using the information available from the smallest resolved scales[13].[13] suggests to make use of a test filter with width larger than the original filter and employ the same model to calculate the sub-grid scale stresses τ_{ij} and the stresses T_{ij} resulting from this additional filter, and eventually predicting CL^2 where C equals to C_s^2 .

The Wall-Adapting Local Eddy-viscosity (WALE) model [19]uses information from the traceless symmetric part of the resolved velocity gradient tensor g_{ij} to calculate the eddy viscosity(Equation 15):

$$\nu_t = (C_w \Delta)^2 \frac{\left|G_{ij}^a\right|^{6/2}}{\left(\bar{S}_{ij}\bar{S}_{ij}\right)^{5/2} + \left|G_{ij}^a\right|^{5/2}} \tag{15}$$

where G_{ij}^a is the traceless part of the resolved velocity gradient tensor. C_w is a model constant with values ranging from 0.45 to 0.5 based on the information extracted from simulations of isotropic homogenous turbulence [19]. More recent developments include scale-dependent dynamic models for anisotropic grids and implicit LES (ILES) approaches in which the numerical discretization provides part of the SGS dissipation [27]. While FLOW-3D implements the classical Smagorinsky formulation, these modern advancements provide useful context for interpreting LES performance and limitations in complex hydraulic simulations.

3.1.3 Turbulent Boundary Layer

Most turbulent flows are influenced by viscous boundary layers that can be extremely thin, making them impractical to resolve using standard finite difference or finite volume grids, especially in three dimension.An alternative approach is to use wall function to model the inner unresolved layer based on the behaviour of the outer resolved layer.Values of wall shear stress τ_w and turbulent scalars k_T , ϵ_T in the wall adjacent cells are coupled to the mean flow through algebraic functions [12].

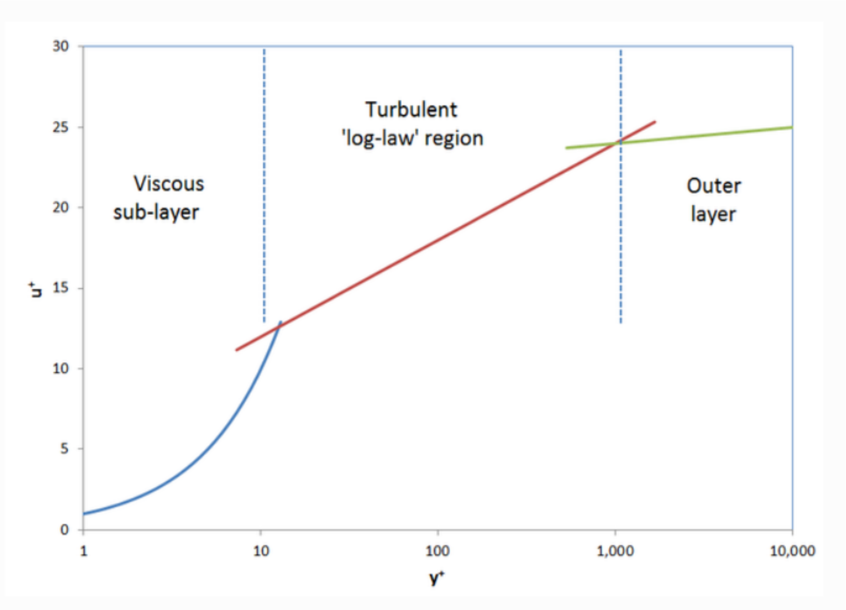

Figure 3: Dimensionless Turbulent Velocity Regions

The dimensionless near-wall turbulent velocity profile $u_+ = \mathrm{f}(y_+)$ is universal and can be broken into (at least) three regions as shown in the figure 3 . In the viscous sub-layer (y_+ less than 5), turbulent fluctuations are suppressed by the close proximity of the wall and the flow is laminar. Conversely, far from the wall, in the outer layer, the boundary layer scaling is controlled mostly by the inertial core of the mean flow and direct viscous effects are absent [12]. In between is the log-law region where turbulent stresses (the Reynolds stresses) dominate. Here, mixing length theory results in a logarithmic relationship between u_+ and y_+ given by (Equation 17):

$$u_+ = \frac{u}{u_*}, \quad y_+ = \frac{\rho_f \, u_* \, d}{\mu_f}, \quad u_* = \sqrt{\frac{\tau_w}{\rho_f}} \tag{16}$$

$$\frac{u}{u_*} = \frac{1}{\kappa} \ln\left(\frac{\rho_f \, u_* \, d}{\mu_f}\right) + 5.0 \tag{17}$$

where u and u_* are the tangential and friction velocities for the wall , and $\kappa = 0.4$ is the von Karman constant.

In FLOW-3D HYDRO , the influence of surface roughness with height k on the turbulent boundary layer is modelled with an extra contribution to the viscosity. When that happens , the definition of y_+ in Eq. 17 becomes:

$$y_+ = \frac{\rho_f \, u_* \, d}{\mu_f + \alpha \rho_f \, u_* \, k} \tag{18}$$

where $\alpha = 0.246$ is a constant that makes the expression consistent with the formula for rough wall turbulent flows [29] .

3.2 Sediment Transport Model

To model the sediment transport phenomenon, multiple non cohesive sediment species can be assumed with different properties such as grain size, mass density, critical shear stress , angle of repose and entrainment and transport parameters.This model can be used for both 3D and shallow water flows(typically used to simulate flows in rivers).The motion of the sediment consists of erosion, advection and deposition.The model computes the following to track the motion of sediments:

- transport of suspended sediments.
- settling of sediment due to gravity.
- sediment entrainment due to bed shear and flow perturbations.
- bed load transport by rolling, hopping or sliding along the packed sediment bed.

The sediment can can modelled to be in two conditions, suspended and packed bed. Suspended sediments move along with the mean flow while the packed bed with a certain packing fraction stays at a specific desired position and only a layer of it is transported in the form of bed load transport.

The entrainment of sediment occurs by the picking up and resuspension due to shear and small eddies at the upper bound of the packed bed. An empirical model is used to compute the overall entrainment since it is not possible to track each particle individually.The model used is based on the works of Mastbergen and Van den Berg [16].To determine the critical Shields parameter, the Soulsby-Whitehouse equation [30] can be used or a user-specific value can be specified.The default value is 0.05.The Soulsby-Whitehouse equation for the dimensionless critical Shields parameter is(Equation 19):

$$\theta_{cr,i} = \frac{0.3}{1 + 1.2 d_{*,i}} + 0.055 \left[1 - \exp(-0.02 d_{*,i})\right] \tag{19}$$

where $d_{*,i}$ is the dimensionless parameter which can be evaluated as(Equation 20) :

$$d_{*,i} = d_i \left[\frac{\rho_f(\rho_i - \rho_f)\|\mathbf{g}\|}{\mu_f^2}\right]^{\frac{1}{3}} \tag{20}$$

where ρ_i is the density of the sediment species, ρ_f is the fluid density, d_i is the sediment diameter, μ_f is the dynamic viscosity of the fluid, g is acceleration due to gravity.The local Shields parameter can be computed from the local bed shear stress, τ (Equation 21):

$$\theta_i = \frac{\tau}{\|\mathbf{g}\| d_i(\rho_i - \rho_f)} \tag{21}$$

The entrainment lift velocity of sediment can be computed as[16] (Equation 22):

$$u_{\mathrm{lift},i} = \alpha_i n_s d_*^{0.3} (\theta_i - \theta'_{cr,i})^{1.5} \sqrt{\frac{\|\mathbf{g}\|\, d_i(\rho_i - \rho_f)}{\rho_f}} \tag{22}$$

where α_i is the entrainment parameter with a value of 0.018 and n_s is the normal to the packed bed interface , pointing outward. This entrainment lift velocity helps in determining the amount of packed bed that converted into suspended sediment.

The suspended sediments can be deposited by either settling due to gravity or coming to rest in bed-load transport. The equation for the settling velocity is given as(Equation 23):

$$u_{\text{settling},i} = \frac{\nu_f}{d_i}\left[(10.36^2 + 1.049 \cdot d_*^3)^{0.5} - 10.36\right] \tag{23}$$

where ν_f is the kinematic viscosity of the fluid. The settling motion is in the direction of the gravity. To take into consideration the particle-particle interaction, the Richardson-Zaki's correlation is applied to the settling velocity as follows(Equation 24):

$$u^*_{\text{settling},i} = u_{\text{settling},i}(1 - min(0.5, c_s))^{\zeta} \tag{24}$$

where c_s is the total volume fraction of the suspended sediment. ζ is (Equation 25):

$$\zeta = \zeta_{\text{user}} \cdot \zeta_0 \tag{25}$$

ζ_{user} is the Richardson-Zaki coefficient multiplier and ζ_0 is the main coefficient defined based on the particle Reynolds number. For Reynolds number greater than 500, the value is 2.39 .For bed-load transport, any one of the following three equations can be chosen, which give the volumetric transport rate of sediment per width of the bed:

- Meyer, Peter and Muller [17] (Equation 26)

$$\Phi_i = \beta_{\text{MPM},i}(\theta_i - \theta'_{cr,i})^{1.5} c_{b,i} \tag{26}$$

- Nielsen [20] (Equation 27)

$$\Phi_i = \beta_{\text{Nie},i}\theta_i^{0.5}(\theta_i - \theta'_{cr,i}) c_{b,i} \tag{27}$$

- Van Rijn [22] (Equation 28)

$$\Phi_i = \beta_{\mathrm{VR},i} d_{*,i}^{-0.3} \left[\frac{\theta_i}{\theta'_{cr,i}} - 1 \right]^{2.1} c_{b,i} \tag{28}$$

where $\beta_{\mathrm{MPM},i}$, $\beta_{\mathrm{Nie},i}$,$\beta_{\mathrm{VR},i}$ are coefficients with values of 8.0 , 12.0 and 0.053 respectively.$c_{b,i}$ is the volume fraction of the sediment species i in the bed. The volumetric bed-load transport rate $q_{b,i}$ is related to the dimensionless bed-load transport rate ϕ_i by (Equation 29):

$$q_{b,i} = \Phi_i \left[\|\mathbf{g}\| \left(\frac{\rho_i - \rho_f}{\rho_f} \right) d_i^3 \right]^{\frac{1}{2}} \tag{29}$$

To estimate the bed-load thickness(thickness of the saltating sediment), the equation which can be used is[22] (Equation 30):

$$\frac{\delta_i}{d_i} = 0.3 d_*^{0.7} \left[\frac{\theta_i}{\theta'_{cr,i}} - 1 \right]^{0.5} \tag{30}$$

For the motion of the sediment in each computational cell, the value of $q_{b,i}$ is used to calculate the bed-load velocity $u_{\mathrm{bedload},i}$ (Equation 31) :

$$u_{\mathrm{bedload},i} = \frac{q_{b,i}}{\delta_i c_{b,i} f_b} \tag{31}$$

where f_b is the critical packing fraction of the sediment, assumed to be 0.64. To calculate the suspended sediment concentration for each species i , the following transport equation is solved(Equation 32):

$$\frac{\partial C_{s,i}}{\partial t} + \nabla \cdot (\mathbf{u}_{s,i} C_{s,i}) = \nabla \cdot \nabla (D C_{s,i}) \tag{32}$$

where $C_{s,i}$ is the suspended sediment concentration of species i , defined as sediment mass per unit volume of sediment-fluid mixture; D is the diffusivity;$\mathbf{u}_{s,i}$ is the suspended sediment velocity. The velocity for each species of sediments is different.In order to solve for $C_{s,i}$, the sediment velocity needs to be calculated as(Equation 33):

$$\mathbf{u}_{s,i} = \bar{\mathbf{u}} + \mathbf{u}_{\text{settling},i}\, c_{s,i} \tag{33}$$

where $\bar{\mathbf{u}}$ is velocity of the fluid-sediment mixture.

The sediment transport model has inherent limitations and is not applicable to cohesive soils such as silts and clays. Its use with very coarse sediment should be approached with caution, as the underlying theory may not hold under such conditions. Given the empirical basis of the sediment model and the approximations involved,particularly in the turbulence formulations,parameter calibration may be necessary to optimize performance and ensure reliable results in practical applications.

3.3 Meshing and Boundary Conditions

FLOW-3D HYDRO uses a structured mesh that maybe defined in either Cartesian or Cylindrical coordinate system. The geometries interact with the mesh using the FAVOR method, an acronym for Fractional Area/Volume Obstacle Representation. This method computes the open area fractions on the cell faces along with the open volume fraction and reconstructs the geometry based on these parameters.This approach offers a simple and accurate way to represent complex surfaces in the domain without requiring a body-fitted grid [12].

For the meshing of the numerical domain, Cartesian coordinate system and three linked mesh blocks were used. The use of multiple mesh blocks was advantageous since the grid size could be adjusted such that finer cells were produced in the areas of interest ,i.e. the intake pipe and the narrow channel, which were meshed using Mesh Block 3 and Mesh block 2 respectively.The lake of the domain was meshed using Mesh Block 1. The details for all these three mesh blocks can be found in the table 1.

Table 1: Properties of Mesh Blocks

Mesh Block	**Region**	**Average Cell Size**(m)	**No. of Cells**
1	Upward/Downward Lake	2.4	376200
2	Channel	1.2	646400
3	Intake Pipe	1.2	1980

A detailed view of the mesh blocks is shown in figure 4.

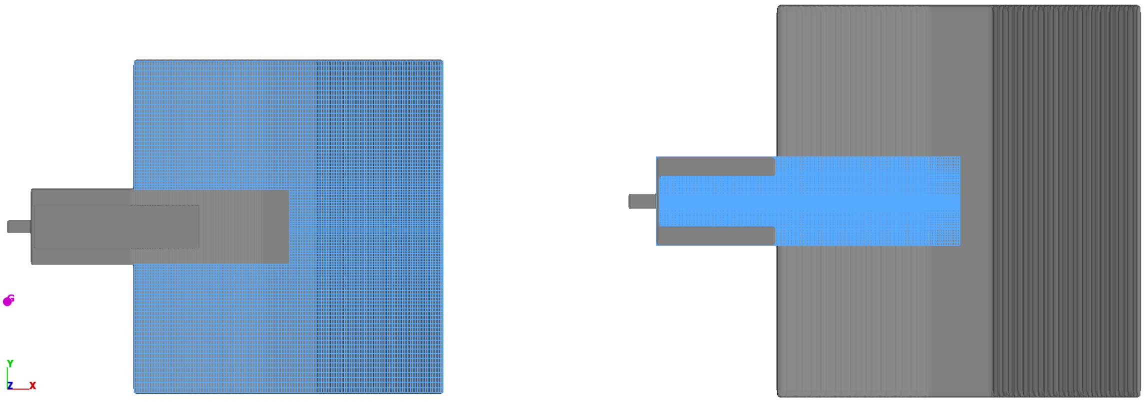

(a) Mesh Block 1-Lake

(b) Mesh Block 2-Channel

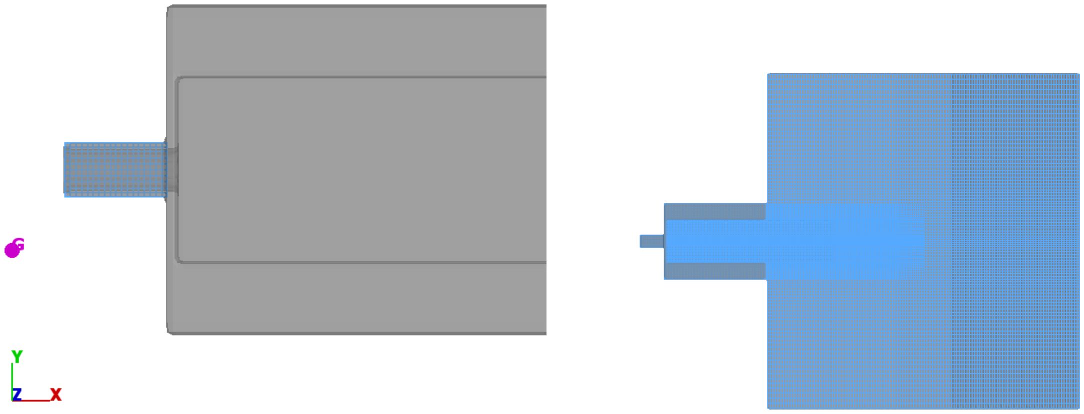

(c) Mesh Block 3-Intake Pipe

(d) Overall Mesh Block

Figure 4: Linked Mesh Blocks in the Computational Domain .

The boundary conditions for the different mesh blocks are specified in Table 2 below.The meaning of each boundary condition used is explained below:

- Symmetry: Applies a zero-gradient condition at the boundary as well as a zero velocity condition normal to the boundary.
- Velocity, Fluid Fraction: A certain velocity of the fluid can be specified at that boundary, meaning a certain volumetric flow rate if multiplied with opening area. Fluid fraction is used to specify the value for the fraction of the fluid entering that boudary. A fluid fraction of 1 means that water fully enters through the boundary. A fluid fraction of 0 means there is no water beyond the boundary.
- Stagnation Pressure, Fluid Elevation: A stagnation pressure condition assumes stagnation conditions outside the boundary so that the velocity upstream(above) from the boundary is zero.A certain pressure at the boundary can also be specified. If the fluid elevation is also specified, the pressure at the boundary will follow a hydrostatic distribution.
- Wall: Applies the no-slip condition at the boundary as well as a zero velocity condition normal to the boundary.

Boundary	**Mesh Block 1**	**Mesh Block 2**	**Mesh Block 3**
Xmin	Symmetry	Symmetry	Velocity Fluid Fraction = 1
Xmax	Symmetry	Symmetry	Symmetry
Ymin	Stagnation Pressure Fluid Elevation = 66.6 m	Symmetry	Wall
Ymax	Stagnation Pressure Fluid Elevation = 66.6 m	Symmetry	Wall
Zmin	Symmetry	Symmetry	Wall
Zmax	Stagnation Pressure Fluid Fraction = 0	Stagnation Pressure Fluid Fraction = 0	Wall

Table 2: Boundary conditions for the mesh blocks.

The initial conditions for all the simulations were specified as Hydrostatic Pressure with a Fluid Elevation of 66.6 m from the bottom of the whole domain, meaning a fluid height of 25 m in the channel and 61.6 m in the lake.

3.4 Simulation Progression

The simulations progressed in the following manner based on the results of consecutive simulations:

- Initial simulations were performed to calibrate the optimal grid size and surface roughness parameters. It was concluded that a cell size of 1 m was optimal and three different surface roughnesses could be chosen: 0.01 m,0.05 m and 0.1 m . The shear velocities near the walls were higher for higher values of roughness, so finally 0.05 m was selected to be used for further simulations.
- A number of simulations were performed with the initial primitive design , but based on results it was observed that the reservoir was in need of expansion , especially in Y-direction. Also, the inlet pipe needed to be pre-expanded before reaching the channel so that there would be a steady flow velocity of $3\,\mathrm{m\,s^{-1}}$ when the flow would reach the channel. These considerations were applied and the overall design was optimized for succeeding simulations.
- Using the improved design, a number of simulations were performed to measure the hydraulic parameters such as mean velocity field, turbulent kinetic energy, shear stresses, vortex structures and recirculation zones. These simulations were performed for both turbining and pumping cases.The cases were simulated until a steady state was reached and required data was extracted using FLOW-3D Post, the post processing software by Flow Science.
- After verifying the hydraulic parameters, the sediment transport model was activated and the channel was modelled as a packed erodible bed of 5 m thickness.For the packed sediment layer, three different sediment sizes with specific volume fractions were chosen, the data for which is shown in Table 3.A number of simulations using this sediment transport model were performed for both turbining and pumping cases.The scouring of packed bed, sediment suspension and deposition patterns

were evaluated.

Table 3: Types and properties of sediments chosen for packed bed

Sediment Type	**Diameter** (m)	**Volume Fraction**(%)	**Density** ($\mathrm{kg\,m^{-3}}$)
Fine Gravel	0.01	25	2650
Intermediate Sand	0.002	50	2650
Fine Sand	0.0005	25	2650

- Two final simulations for the Turbining case: one with the RANS(RNG k-ε) turbulence model and the other with the LES model with a Smagorinsky coefficient of C_s= 0.08 , with the velocity boundary condition of V_x=3.8 m/s at the start of the intake/outlet pipe were performed for validation with the experimental data.Both of these simulations were re-started from a steady state condition which was obtained by running the simulation model with sediment transport deactivated and using RANS turbulence model.Both the simulations used the sediment layer as a packed bed with the aforementioned types of sediments and Sediment Transport model was activated at the start.The results obtained from these two simulations were extracted and used for comparison and validation with the experimental data obtained from the Physical Model.

4 Experimental/Physical Model

The physical model for the reservoirs of the PSH was constructed in the Hydraulic Engineering Laboratory (LIDR) at the Department of Civil, Chemical, Environmental and Materials Engineering (DICAM) in Bologna. The model was scaled to 1:100 (λ= 100) of the numerical model to fit in the existing experimental flume suited to sediment transport modeling in the laboratory. A two-way retrofitted pump acted as a turbine/pump based on the orientation of the valves.

The physical model(Fig.5) replicates all the features of the numerical model, starting upstream with an intake/outlet pipe connecting the intake/outlet structure to the channel. The channel then gives way to the wider lake region downstream. The side walls of the channel use glass in order to maintain roughness parameters. For the bed material initially, coarse gravel is used throughout the channel and the lake in order to properly mount the ultrasound probes for velocity profiling. For the sediment transport experiment, a packed bed of fine sand will be used in the channel to match the packed bed from the numerical model. Froude similarity is adopted and relevant parameters in the model are scaled accordingly. Reynolds number doesn't exactly match when switching from numerical(CFD) model to experimental model, but it is always very large that somehow limits scale effects on the turbulence field. In our case, $\mathrm{Re}_{\mathrm{CFD}}=10^7$ and $\mathrm{Re}_{\mathrm{EXP}}=10^5$, so somehow the Reynolds criteria matches as well. Based on Froude similarity, velocities for the experimental model are scaled down by $\lambda^{1/2}$ from the velocities implemented in the numerical model. The shear stresses, hydraulic head and pressure are scaled by λ , meaning that the water level in the experimental model is initially maintained at 25 cm from the channel bed ,also corresponding to pipe invert elevation, for the turbining and pumping experiments.

(a) Axial Probes with Intake/Outlet (b) Top View

(c) Side View with Horizontal Probes (d) 3D View

Figure 5: Scaled Physical Model of the Reservoir constructed at the LIDR Lab , UNIBO .

An Ultrasonic Velocity Profiler(UVP) with probes and a data acquisition software were used to capture the three-dimensional velocity fields with sufficient temporal and spatial resolution(100-200 Hz and 1-3 mm, depending on the probe).Three primary measurement locations were selected.The first probe was placed with a Doppler angle of 70° on the pipe ceiling elevation, very close to the intake/outlet section(Fig.5a) to measure the inflow velocity. Four other 4 MHz looking-up probes(Fig.5a), with a slanted(60° Doppler angle relative to the horizontal) and vertical pair were placed along the channel axis, at 1-diameter and 2-diameter positions downstream of the intake section. These probes were placed in the bed of the channel and protruded just enough to gather the data and not disturb the flow. Two other horizontal 1 MHz side-looking probes(Fig.5c) were placed at the left side of the channel behind the glass, aligning with the axial line of the pipe at 1-diameter and 2-diameter. These three probes(slanted , vertical and horizontal) were aligned such that their spatial acquisition lines intersected at two points on the axial line of the intake/outlet section at 1-diameter and 2-diameter.

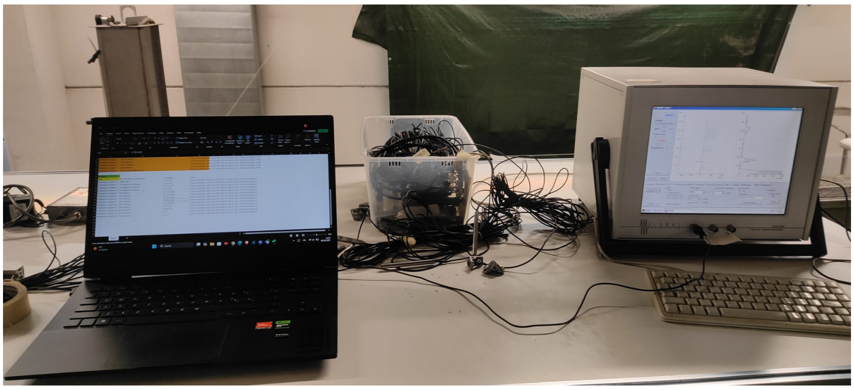

Figure 6: UVP Experimental Setup

The slanted probes were used to measure the streamwise velocity component along the water column. The slanted configuration allows the Doppler beam to intersect the flow direction, enabling accurate reconstruction of the axial velocity through geometric scaling. The vertical probes were used to measure the vertical velocity component along the water column.The horizontal probes, placed laterally were used to measure the horizontal velocity component across the channel.

The UVP(Fig.6)relies on the Doppler effect, in which the frequency of an emitted acoustic pulse shifts when it is scattered by particles or micro-bubbles moving with the fluid. The frequency shift δf is proportional to the component of the particle velocity along the beam direction(Equation 34):

$$u = \frac{c\,\Delta f}{2\,f_0\,\cos\theta} \tag{34}$$

where c is the velocity of sound in water, f_0 is the emitted frequency and θ is the beam angle relative to the flow direction(Doppler angle). Because particles and micro-bubbles act as acoustic scatterers, the Doppler signal provides a continuous measurement of velocity without requiring seeding.Although , a bubble generator was used upstream of the probes to increase the resolution of the signals.

The UVP system emits pulses along a narrow beam and reconstructs a vertical velocity profile by sampling multiple depth cells along the beam path. This allows the measurement of velocity as a function of depth, capturing shear layers, near-bed deceleration, and vertical flow structures associated with scour development [32].

The details related to the experiment concerning the acquisition of the velocity profiles are provided in table 4.The parameters mentioned in the table are clarified below:

File	**Valve**	**Probe**	**Freq.**	**Pos.**	**Alignment**	**DA**	**PRF/PRI**	**TGC**	**Profile Res.**	**Time Res.**
T4_0	20.5 CW	0	4 MHz	Pipe	Vertical	70°	5000 Hz / 200 µs	41	1.11	0.21
T4_1	20.5 CW	1	4 MHz	1 Dia	Vertical	60°	4545 Hz / 220 µs	20–37	1.11	0.01
T4_2	20.5 CW	2	4 MHz	1 Dia	Vertical	90°	3571 Hz / 280 µs	20–37	1.11	0.02
T4_3	20.5 CW	6	1 MHz	1 Dia	Horizontal	0°	1694 Hz / 590 µs	6–23	4.44	0.04
T4_4	20.5 CW	3	4 MHz	2 Dia	Vertical	60°	4761 Hz / 210 µs	20–37	1.11	0.01
T4_5	20.5 CW	4	4 MHz	2 Dia	Vertical	90°	3571 Hz / 280 µs	20–37	1.11	0.02
T4_6	20.5 CW	7	1 MHz	2 Dia	Horizontal	0°	1694 Hz / 590 µs	6–23	4.44	0.02

Table 4: Probe configuration and acquisition parameters

- Valve Opening: The opening of the valve of the retrofitted pump
- Frequency: of the probes
- DA: Doppler Angle for the probes
- PRF/PRI: Pulse Repetition Frequency , the number of acoustic pulses emitted per second, while the Pulse Repetition Interval , the time between two consecutive pulses, i.e., the inverse of the PRF
- Time Gain Compensation(TGC): depth-dependent gain that boosts weaker echoes from farther distances so the whole velocity profile has a consistent signal level
- Profile resolution: vertical (range-wise) spacing between velocity gates along the acoustic beam
- Time resolution: time interval between two consecutive velocity profiles

5 Results and Discussion

5.1 Velocity Profiles

5.1.1 Time Averaged Profiles

The time-averaged velocity profiles provide complementary insight into the mean flow structure and the underlying coherent vortical motions. In the stream-wise direction, both the RANS and LES turbulence models seem quite capable to reproduce faithfully the velocity profiles at intake/outlet, 1-diameter and 2-diameter in comparison to the experimental profiles, with the mean flow and shear layer reasonably reproduced, though minor deviations in peak magnitude remain.

The horizontal velocity profiles are particularly informative, as their pronounced lateral oscillations reflect the presence of horizontal vortex structures rather than simple cross-channel transport. The alternating positive and negative values across the channel width are characteristic signatures of coherent vortices in turbulent shear flows, consistent with classical vortex dynamics in which vorticity is convected, stretched, and transported within the flow field [18]. The spacing between successive zero crossings in the experimental profiles provides an estimate of the vortex wavelength, and both RANS and LES models reproduce this spacing reasonably well, indicating that the numerical model captures the dominant horizontal vortex scale even if the amplitudes differ. Similar relationships between vortex wavelength and flow structure have been documented in studies of undulated or vortex-generating geometries, where the imposed wavelength strongly influences the resulting vortex pattern and turbulence distribution [15].

The time-averaged vertical-velocity profiles (Fig. 7e and Fig. 7f) reveal that both RANS and LES are able to reproduce the overall gradient and curvature observed in the experiments, indicating that the dominant secondary-flow mechanisms are captured by both turbulence models. However, important differences emerge in the magnitude and shape of the predicted profiles. The RANS model consistently produces larger vertical-velocity magnitudes than both the LES and the experimental measurements, suggesting an over-prediction of the secondary circulation strength. In contrast, the LES profiles follow the experimental curves more closely across the entire depth, particularly in the mid-depth region of shear layer . Overall, while both models capture the general behaviour of the vertical-velocity field, LES reproduces the experimental profiles more faithfully, whereas RANS exaggerates the magnitude of the vertical motion despite matching the overall gradient.

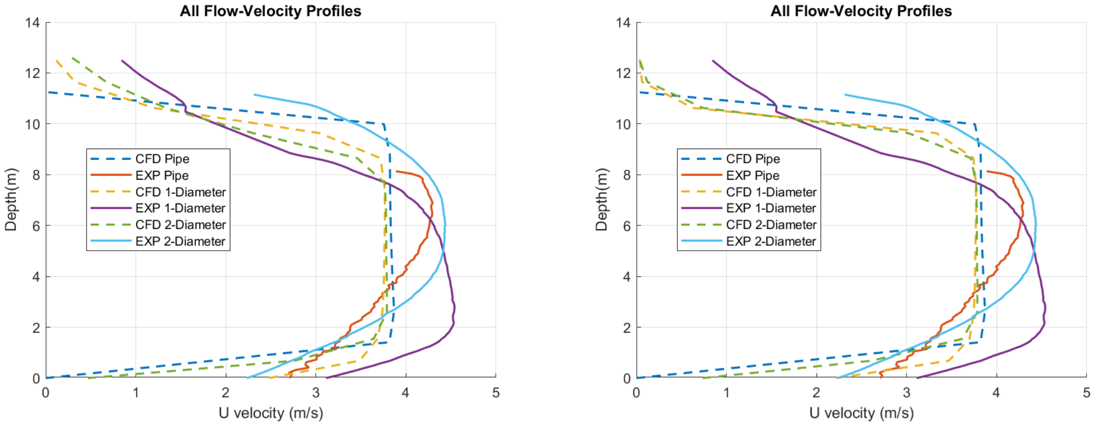

(a) Experimental vs RANS (b) Experimental vs LES

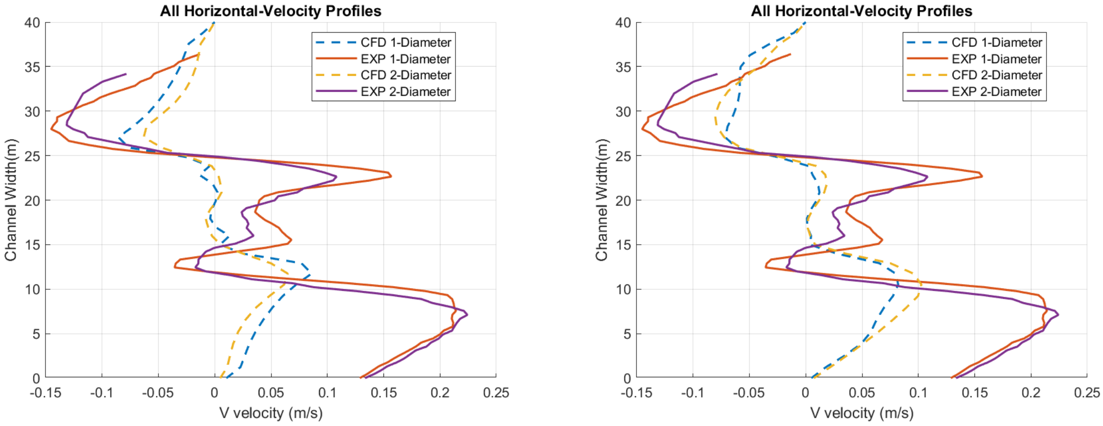

(c) Experimental vs RANS (d) Experimental vs LES

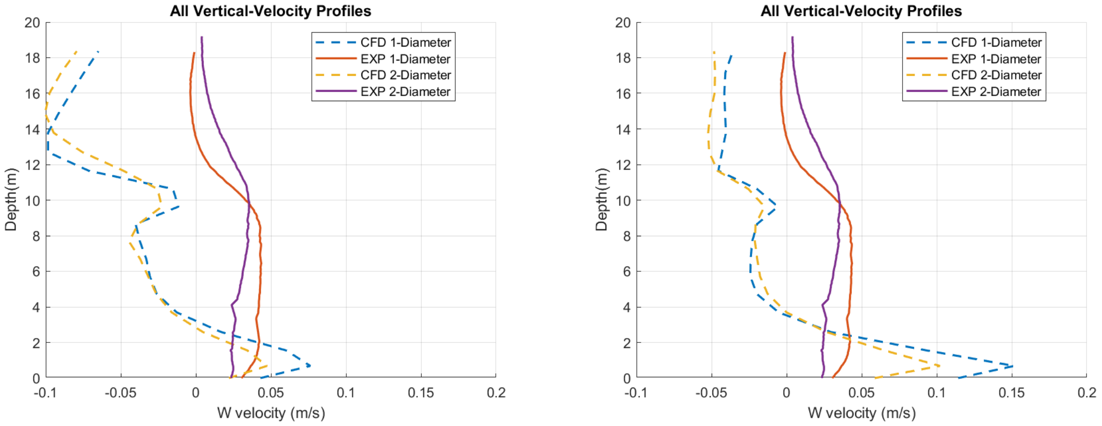

(e) Experimental vs RANS (f) Experimental vs LES

Figure 7: Time Averaged Velocity Profiles at Different Positions-Experimental vs RANS and LES

5.1.2 Instantaneous Profiles

Streamwise (Flow) Velocities Since no relevant difference was observed between RANS and LES models in terms of instantaneous flow(streamwise) velocity profiles, a direct comparison between results from LES model and Experimental data is performed as below(Figure8):

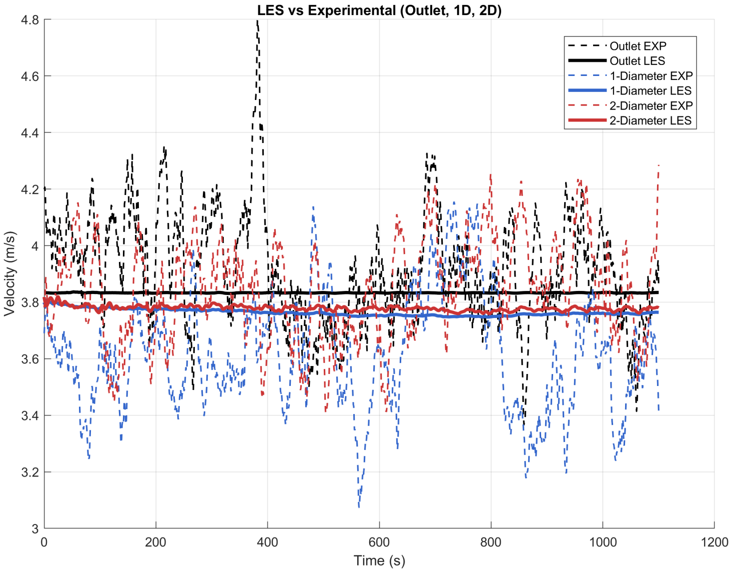

(a) Velocity Profile

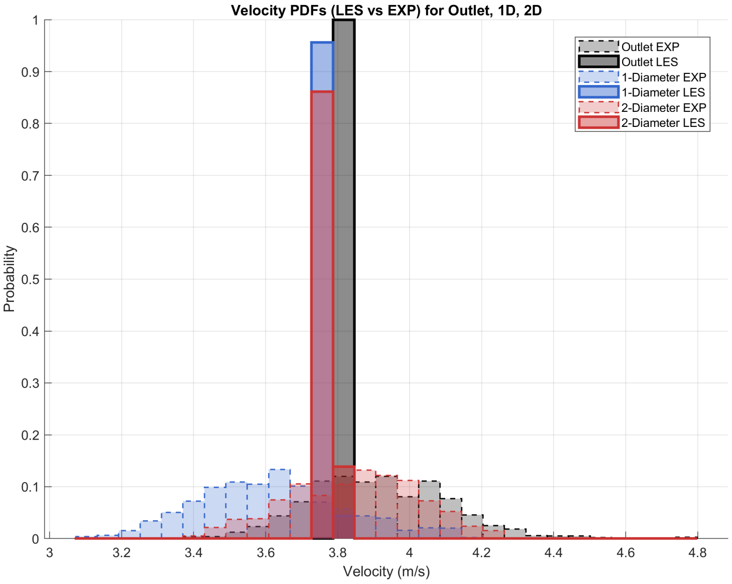

(b) Velocity Distribution PDF

Figure 8: Instantaneous Flow Velocities at Different Positions- LES vs Experimental

The instantaneous streamwise velocities exhibit the strongest temporal variability and the clearest contrast between LES model and experimental behaviour. At the outlet section (see Fig. 8a), the experimental signal shows pronounced fluctuations and intermittent peaks, whereas the LES profile remains comparatively smooth, with a narrower probability distribution centred around a dominant velocity (Fig. 8b). This discrepancy reflects the turbulent inflow conditions in the physical model which was not the case of CFD boundary condition at pipe inflowing velocity. The experiments are subjected to introduced turbulent energy by the laboratory recirculating system (i.e., pump and pipes). As a result, the experiment contains unbalanced and highly energetic motions that the neither of the CFD models can reproduce. Moving downstream to one and two diameters , a similar trend follows with the numerical models unable to replicate the oscillating behaviour of the flow represented by the experimental model.In order to promote this oscillating patterns, numerical simulations need to be set up imposing oscillating boundary conditions that in addition reflects reliable content of turbulent energy in a real prototype.

Horizontal Velocities The horizontal velocity components display a different pattern, with much closer agreement between LES model and experiment at both downstream locations. The instantaneous time series at one and two diameters (Figs. 9a and 9b) show small-amplitude oscillations , and both the numerical models reproduce the sign changes and general temporal structure of the experimental signal.The LES model is able to replicate the experimental signal more faithfully as is evident from the corresponding probability distributions (Figs. 10a and 10b). The distributions are very narrow for the RANS model while the LES distribution is wide enough to almost capture the full velocity spectrum of the experimental model.One of the reasons for this might be because LES can resolve the large eddies while modelling the smaller eddies(sub-grid scale) while the RANS model is unable to do so.

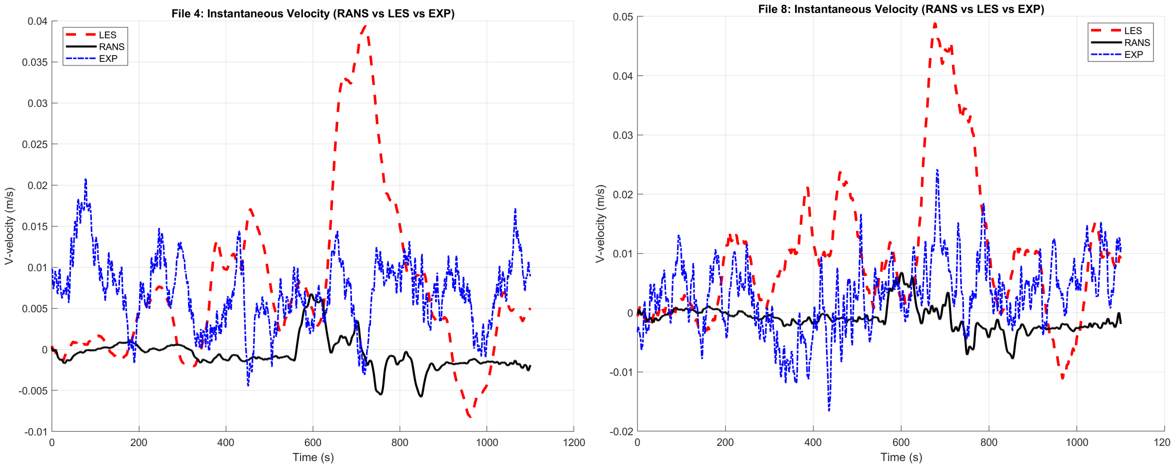

(a) 1-Diameter from I/O (b) 2-Diameter from I/O

Figure 9: Instantaneous Horizontal Velocities at Different Positions-RANS vs LES vs Experimental

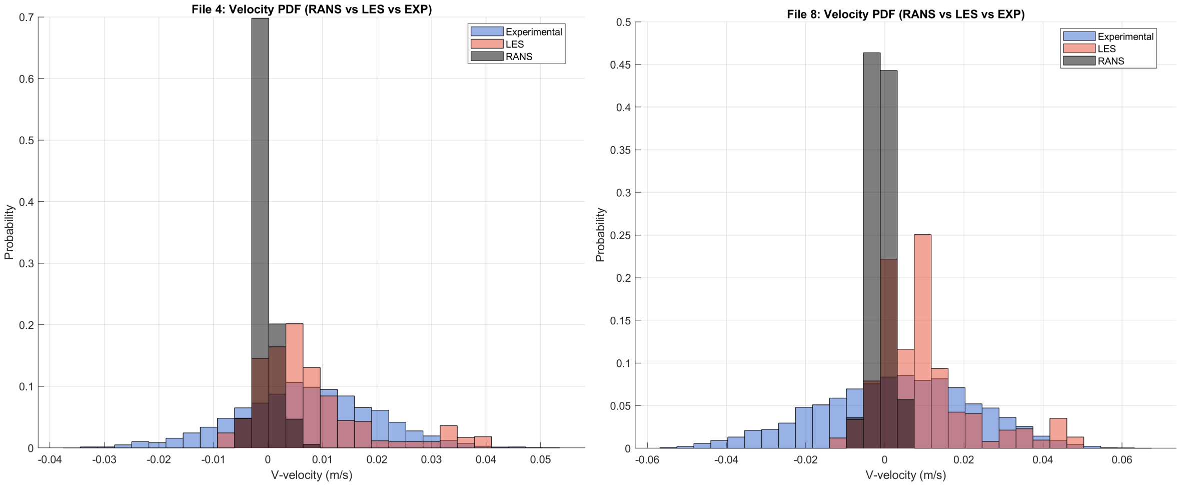

(a) 1-Diameter from I/O (b) 2-Diameter from I/O

Figure 10: Instantaneous Horizontal Velocity PDF at Different Positions- RANS vs LES vs Experimental

Vertical Velocities The vertical velocity components are better represented by both the numerical models at both locations. At one diameter downstream(Figs. 11a and 12a), the experimental signals display more pronounced intermittency and a broader probability distribution which is reproduced with great fidelity by the LES model, while the RANS model overpredicts the upward motion(positive values). At two diameters downstream, the instantaneous time series(Fig. 11b) and the corresponding probability distributions(Fig. 12b) show a similar trend with the velocity distribution from LES model matching more closely with the experimental profile and distribution. This suggests that the LES turbulence model is better suited to represent the vertical velocity fluctuations in the shear layer developing between inflowing momentum and the above water volume covering the inflow pipe. LES approach resolves the large eddies of the shear vertical layer scaled with pipe diameter and water depth, while it models smaller scales in a sub-grid approach.

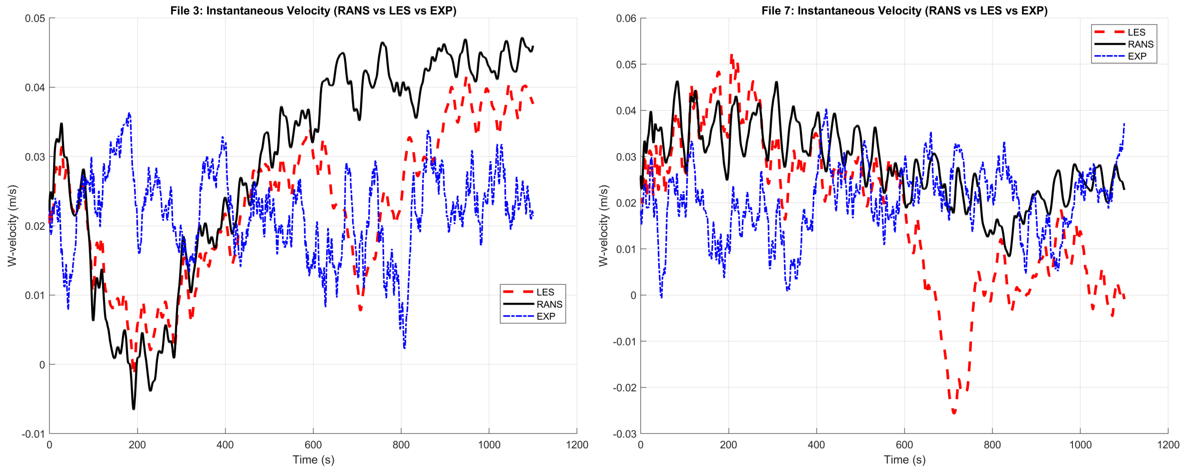

(a) 1-Diameter from I/O (b) 2-Diameter from I/O

Figure 11: Instantaneous Vertical Velocities at Different Positions- RANS vs LES vs Experimental

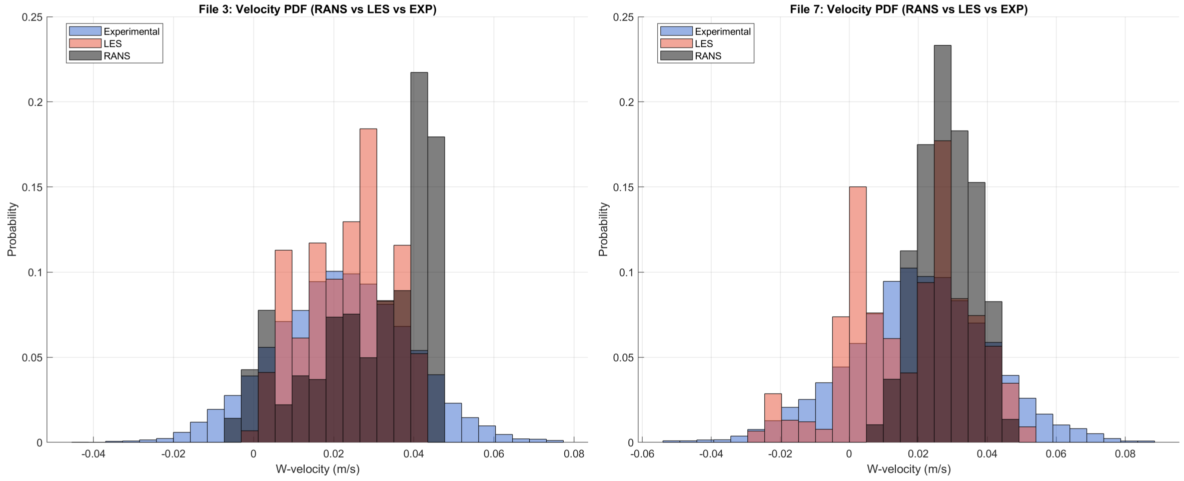

(a) 1-Diameter from I/O (b) 2-Diameter from I/O

Figure 12: Instantaneous Vertical Velocity PDF at Different Positions- RANS vs LES vs Experimental

5.2 Statistical Metrics

To quantify the agreement between the numerical (CFD) and experimental instantaneous velocity signals, several standard statistical metrics were computed. Let $u_{\text{EXP}}(t)$ denote the experimental velocity and $u_{\text{CFD}}(t)$ the numerical velocity interpolated onto the same time vector.

Relative Mean Absolute Error (RMAE) Measures the average absolute deviation relative to the experimental velocity(Equation 35):

$$\text{RMAE} = \frac{1}{N}\sum_{i=1}^{N}\left|\frac{u_{\text{CFD}}(t_i) - u_{\text{EXP}}(t_i)}{u_{\text{EXP}}(t_i)}\right| \tag{35}$$

Relative Root Mean Square Error (RRMSE) Penalizes larger deviations, normalized by the experimental velocity(Equation 36):

$$\text{RRMSE} = \sqrt{\frac{1}{N}\sum_{i=1}^{N}\left(\frac{u_{\text{CFD}}(t_i) - u_{\text{EXP}}(t_i)}{u_{\text{EXP}}(t_i)}\right)^2} \tag{36}$$

Correlation Coefficient (R) Measures similarity in the temporal behaviour of the two signals(Equation 37):

$$R = \frac{\text{cov}(u_{\text{CFD}}, u_{\text{EXP}})}{\sigma_{\text{CFD}}\,\sigma_{\text{EXP}}} \tag{37}$$

Values close to 1 indicate that CFD captures the experimental fluctuations well.

Turbulence Intensity (TI) Quantifies the strength of velocity fluctuations relative to the mean(Equation 38):

$$\text{TI}_{\text{EXP}} = \frac{\sigma_{\text{EXP}}}{\overline{u}_{\text{EXP}}}, \qquad \text{TI}_{\text{CFD}} = \frac{\sigma_{\text{CFD}}}{\overline{u}_{\text{CFD}}} \tag{38}$$

Comparing TI indicates how well CFD reproduces the turbulence level.

The statistical indicators from the Table 5 validate the observations made in the previous sections . The largest deviations between the experimental and both numerical

Table 5: Statistical comparison between Experimental, RANS and LES instantaneous velocities.

Velocity	RANS			LES		
	RMAE(%)	RRMSE(%)	R	RMAE(%)	RRMSE(%)	R
I/O-Flow	25.08	25.08	0.0258	25.08	25.08	0.0417
1Dia-Flow	2.67	2.68	-0.0336	2.75	2.77	-0.0479
1Dia-Vertical	266.77	282.49	-0.0955	238.25	247.49	-0.0326
1Dia-Horizontal	103.41	104.78	-0.0563	74.74	84.73	-0.0347
2Dia-Flow	13.86	13.87	0.0242	13.78	13.79	-0.0069
2Dia-Vertical	31.45	37.74	-0.0128	66.96	80.18	-0.0452
2Dia-Horizontal	104.53	106.03	0.0655	74.88	83.13	0.0643

Table 6: Turbulence intensity comparison between Experiment, RANS and LES.

Velocity	TI_EXP	TI_RANS	TI_LES
I/O-Flow	0.190	0.0004	0.0005
1Dia-Flow	0.147	0.003	0.0033
1Dia-Vertical	0.775	0.557	0.4848
1Dia-Horizontal	1.895	-4.962	1.3444
2Dia-Flow	0.142	0.005	0.0056
2Dia-Vertical	1.026	0.382	1.3227
2Dia-Horizontal	7.336	-3.928	1.4265

datasets(RANS and LES) is observed at the intake/outlet section , with both RMAE and RRMSE exceeding 0.25. The vertical and horizontal components have accentuated errors due to the fact that the experimental velocity values are lower than the numerical ones . Correlation coefficients remain low across all locations, ranging from approximately -0.02 to 0.09, indicating that the CFD model struggles to reproduce the temporal structure of the fluctuations.

Turbulence intensity(Tab.6) is well predicted for horizontal and vertical velocities, but underpredicted for the flow velocities, the reason being different boundary conditions, non-oscillating for the RANS and LES models and oscillating turbulent inflow velocity for the experiment. Overall, the LES model matches the experimental turbulence intensity behaviour with high fidelity, especially in horizontal and vertical directions at 1-diameter and 2-diameter positions.

5.3 Sediment Transport

5.3.1 Shear Stress

The maximum shear-stress distribution at the channel bed (Fig. 13) highlights clear differences in how RANS and LES represent near-bed momentum transfer. In the immediate vicinity of the intake/outlet structure, both models predict a strong mean-shear zone generated by the high-velocity jet, and the agreement between the two approaches is relatively close. Further downstream, however, the models diverge. The RANS solution maintains a narrow, axis-aligned band of elevated shear stress that follows the core of the mean flow, reflecting the well-known tendency of eddy-viscosity RANS closures to over-smooth turbulence and suppress anisotropic shear production [23]. In contrast, the LES field exhibits a laterally broader and more irregular distribution of maximum shear stress. This widening is associated with the resolved turbulent eddies that transport momentum sideways, producing localized shear patches that RANS cannot capture due to its reliance on isotropic turbulence assumptions [11, 31].Such differences are highly relevant for sediment-transport modelling, as bedload motion, scour initiation, and sediment suspension are strongly governed by the spatial variability of near-bed shear stress . Consequently, the LES prediction provides a more physically realistic representation of the shear-stress footprint influencing sediment dynamics, whereas RANS captures the general trend but under-represents the lateral spreading of high-shear zones.

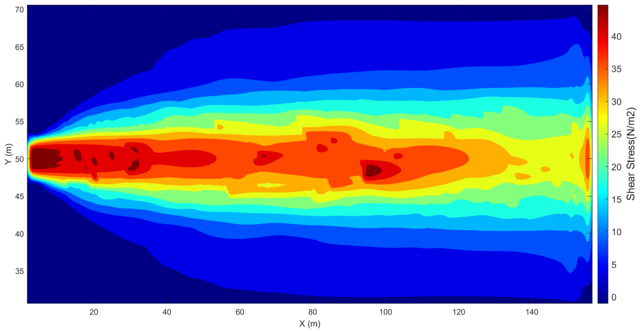

(a) RANS

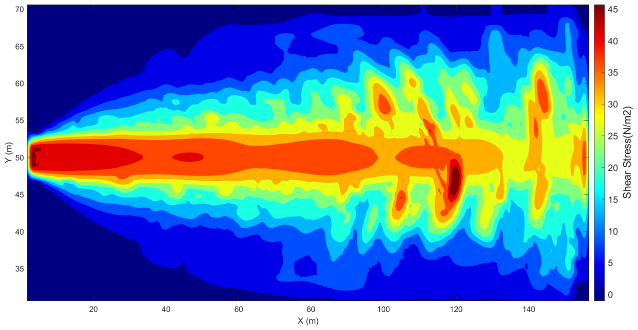

(b) LES

Figure 13: Maximum Shear Stress Distribution in the Channel

Figure 14 shows the comparison between RANS and LES model of instantaneous shear stresses very close to the channel bottom(boundary layer) for 1-diameter and 2-diameter axial locations downstream of the outlet section and for loose(erodible) bed simulations. At 1-diameter downstream, both models predict values of shear stresses around 40 Pa initially, which starts decreasing until midway of the simulation, suggesting scouring of the sediment bed.There is a larger decrease in the stress obtained from LES at this location, suggesting greater scour development. The shear stresses again start increasing and decrease shortly suggesting re-deposition of the suspended sediments and a secondary scour development. In contrast, at 2-diameter the RANS solution shows more pronounced temporal variability than at 1-diameter, while the LES signal remains comparatively smooth.This variability is more likely associated with turbulence fluctuations. Also the values do not decrease drastically compared to the beginning of the simulation for this location, which suggests that this region is less prone to very deep scour development.

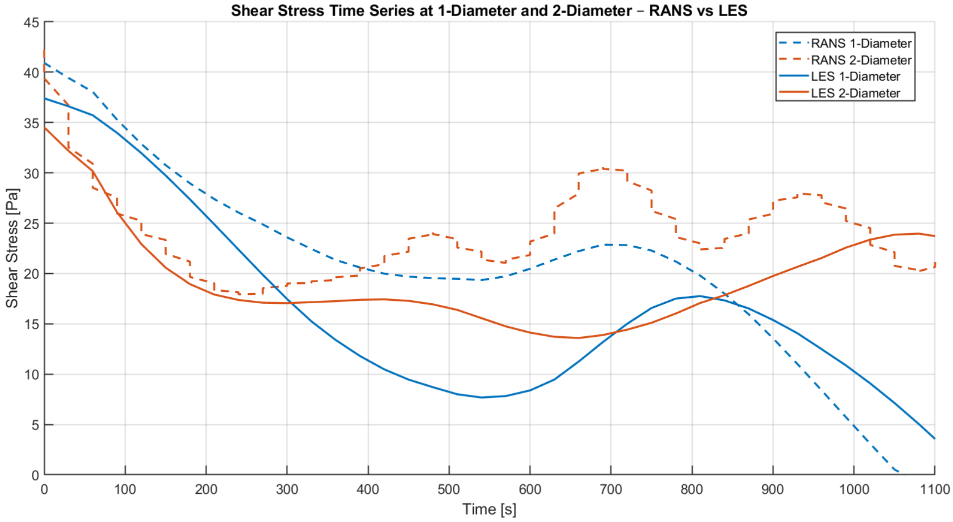

Figure 14: Shear stress time series at 1-Diameter and 2-Diameter for RANS and LES simulations.

The large discrepancy between the experimental and numerical(LES and RANS) values of friction velocities and shear stresses(Table 7) are obtained because of the fundamental difference in the bed roughness of the two systems.In the experimental model, the channel bed is composed of very coarse 10-15 mm gravel (corresponding to 1.0-1.5 m boulders in the numerical prototype) which produces a very rough flow regime and enhanced turbulence momentum exchange near the bed. This yields high values of friction velocities , 0.535 m/s and 0.381 m/s respectively for the 1-diameter and 2-diameter locations, corresponding to shear stresses of 286 Pa and 145 Pa. Even the associated standard errors for the friction velocities remain substantial , reflecting energetic and highly turbulent near-bed flow over the coarse gravel.The use of coarse gravel in the experimental setup is consistent with preliminarily tests objective, namely the characterization of mean flow and turbulent coherent structures with a fixed bed. Then, experimental setup will be further developed with loose bed of fine sand to eventually test sediment mobility under more realistic shear stress conditions.

In contrast , the numerical models use the standard packed bed with three different grain sizes as mentioned in Table 3.This boundary is represented through a wall-function roughness rather than a fully resolved grain geometry.This results in a hydraulically smoother boundary, producing lower friction velocities for the RANS and LES cases. The resulting shear stresses(15-24 Pa) are an order of magnitude smaller than those obtained from the experimental model.

Position	Case	Mean u_* [m/s]	SE u_* [m/s]	Mean τ [Pa]
1-Diameter	Experimental	0.5350	0.0332	286.23
	RANS	0.1434	0.0070	20.56
	LES	0.1235	0.0075	15.26
2-Diameter	Experimental	0.3810	0.0057	145.16
	RANS	0.1557	0.0023	24.24
	LES	0.1404	0.0037	19.72

Table 7: Comparison of experimental and numerical friction velocity statistics.

5.3.2 Sediment Dynamics

The results from the sediment transport simulation using the two different turbulence modelling approaches are compiled in this section. The suspended sediment data over a horizontal plane very near to the channel bed were extracted to produce meaningful plots and curves. The various plots and curves generated are:

- Maximum Suspended Sediment Concentration: Map of maximum values of SSC observed during the entire simulation
- Heat Maps for High Concentration Time Steps: Maps of SSC for time steps with SSC over a certain threshold
- Centroid Evolution in X and Y : evolution of center of mass of the entire suspended cloud in time
- Wavefront Propagation in X and Y : evolution of the point of maximum concentration of suspended sediments in time

These plots and curves were generated for each of the sediment classes mentioned earlier in Table 3 since the packed layer of sediment bed in the channel was composed of all three of these classes of sediments with specific volume fraction mentioned in the table.

The maximum suspended sediment concentration maps for the three different classes of sediments displays substantial difference in sediment transport modelling between RANS and LES. The sediment suspension by the RANS model follows a narrower region aligned to the longitudinal axis of the mean flow and the channel, while that from the LES model is more laterally spread throughout the channel due to the resolved turbulent eddies.

For the Fine Sand class of sediment, the maximum concentration regions are widespread and cover almost the whole domain of the channel. For the RANS simulation, the red core of highest concentration of around 28 kg/m3 (Fig. 15a) indicates the suspension of fine sand by the main flow and subsequent transportation downstream of the channel. Two yellow regions of concentration around 17-18 kg/m3 are observed on either side of the main jet , suggesting recirculation zones or secondary vortices trapping and resuspending sediment lifted from the bed and advected sideways, leading to locally elevated concentrations away from the main axis. From the LES simulation (Fig. 15b), a small axial region of suspension and downstream advection is observed. Also, several large and fragmented structures of sediment accumulation are formed , driven by resolved larger and smaller eddies as well as secondary vortices. These eddies and vortex structures lead to irregular and extended suspension and resuspension patterns and potential scour sideways.

For the Intermediate Sand class, high concentration zones are shifted downstream of the intake/outlet section. From the RANS simulation (Fig. 15c) , the red core of highest concentration of intermediate sand is wider than that observed for fine sand and almost reaches until the end of the channel. This red core is then enveloped by lower concentration regions and the concentrations around the lateral regions to the main flow are almost absent suggesting that the recirculation zones and secondary motions are not powerful enough to keep the intermediate sand in resuspension. Similar trend is seen from the LES simulation (Fig. 15d) with only the large and medium energy eddies being able to suspend and advect sediments downstream and sideways with less lateral spreading. A relatively sharp downstream tongue of high concentration(starting at around 130 m from the intake/outlet) is observed , because of strong velocity gradients created when the flow from the channel transitions down the slope into the wider lake. This region is characterized by high flow acceleration and intensified shear stresses along with flow expansion, promoting the turbulence production and sediment entrainment.

Similarly, for the Fine Gravel class, a very narrow red core of highest concentration centered around the axis is observed , which starts from 40 m downstream of the intake/outlet where the mean flow is the strongest , from the RANS simulation(Fig. 15e). Almost negligible lateral spreading is observed since the lateral eddies do not have sufficient energy to suspend the high inertia gravel or keep them resuspended. From the LES simulation for fine gravel (Fig. 15f) shows a narrow but more irregular concentration zones.LES tries to resolve the intermittent turbulent bursts and localized shear events that produce small lateral patches of high concentrations.This reflects short-term suspension and saltation driven by coherent eddies.But as we move further downstream, the lateral spread of these zones increases significantly. So , one can conclude that the large eddies are able to suspend the sediments but for very sort intervals and then they get deposited back again into the bed.

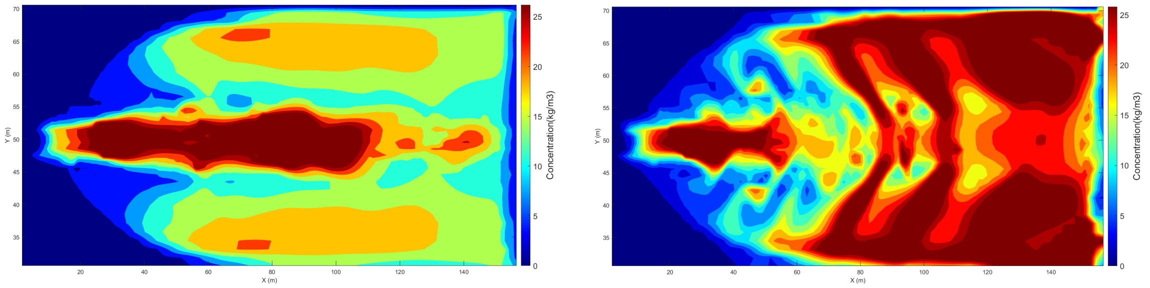

(a) RANS-Fine Sand (b) LES-Fine Sand

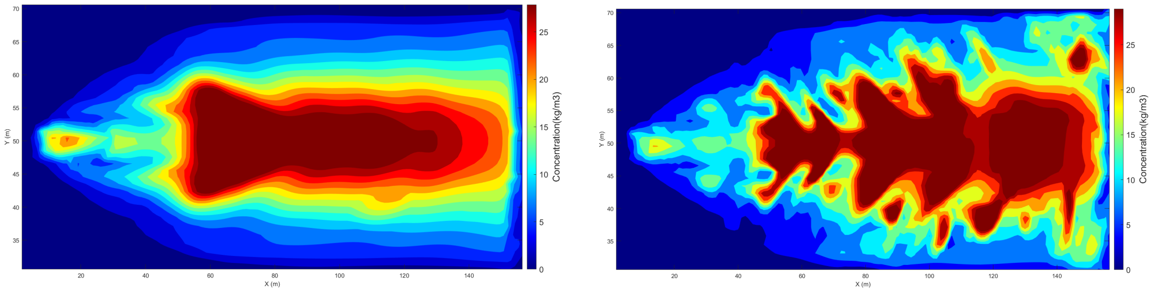

(c) RANS -Intermediate Sand (d) LES-Intermediate Sand

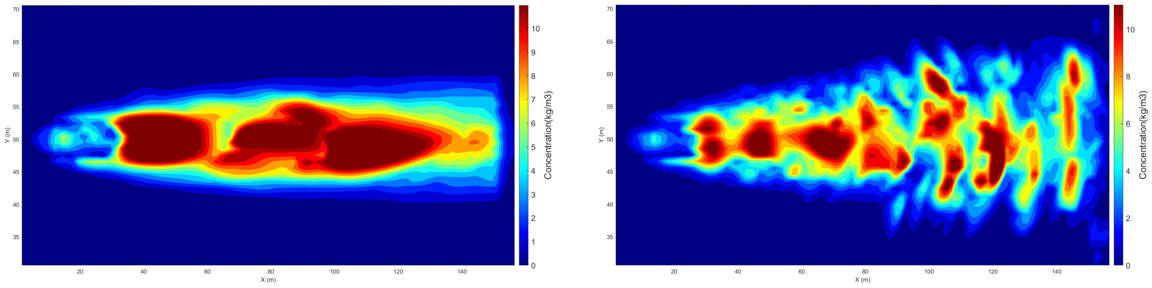

(e) RANS-Fine Gravel (f) LES-Fine Gravel

Figure 15: Maximum Concentration Maps Comparison for Different Sediment Classes

The heat maps for high suspended sediment concentration time steps are consistent with the method of sediment suspension, advection and bed load movement.Since the sediment transport is enable after obtaining a hydrodynamic steady state inside the domain, the mean flow jet, recirculation zones, secondary vortices are already developed for the RANS model. That is why the reproduction of the quality pattern of the maximum concentration map is obtained at a time of 30 s from the start of the simulation for all classes of sediments. Focusing particularly on Fine Sand time steps, the high sediment concentrations are observed along the main jet and slightly lower concentrations laterally close to the channel walls. This axial jet advects the suspended sediment forward towards the lake while the lateral suspensions subside and sediments settle down in subsequent time steps. Small patches suggesting resuspension and advection can be interpreted from the plots(Fig. 16a). Similarly for the LES case(Fig. 16b), multiple fully resolved eddies suspend the sediments throughout the channel and the phenomenon is very random. It is likely that the some sediments are advected into the lake but majority of the sediments appear to be entrained,suspended, resuspended and settled eventually.Similar trends of sediment transport can be observed in successive plots for Intermediate Sand (Fig. 17) and Fine Gravel (Fig. 18), the only difference being the concentrations of suspension, which are higher for the former and lower for the latter.

These qualitative agreements support the theory of the implemented sediment transport scheme.However, full validation of these results is yet to be performed through comparison with measurements from the experimental model,which are planned for the further development of the work in near future.

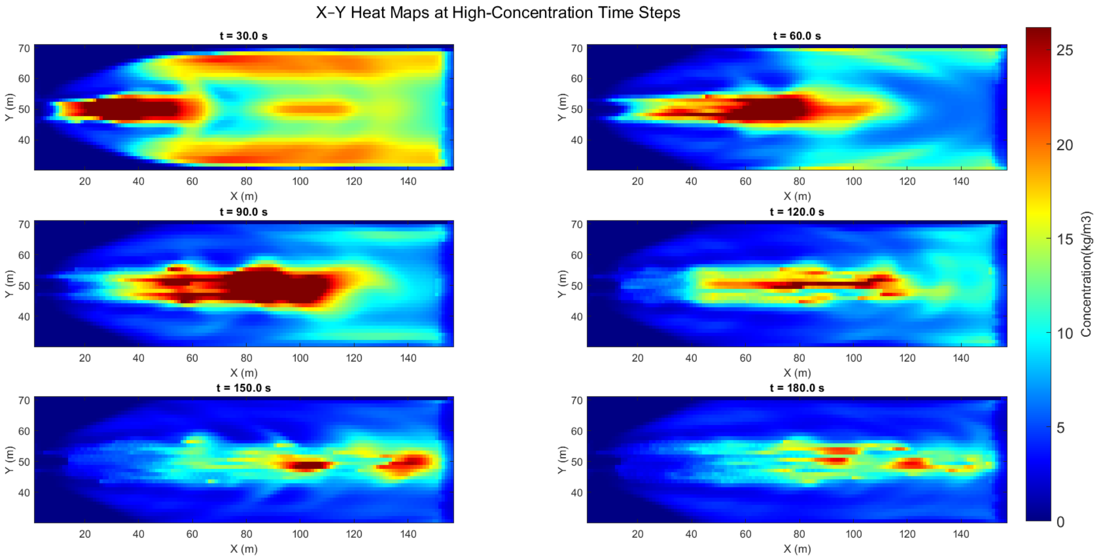

(a) RANS – Fine Sand

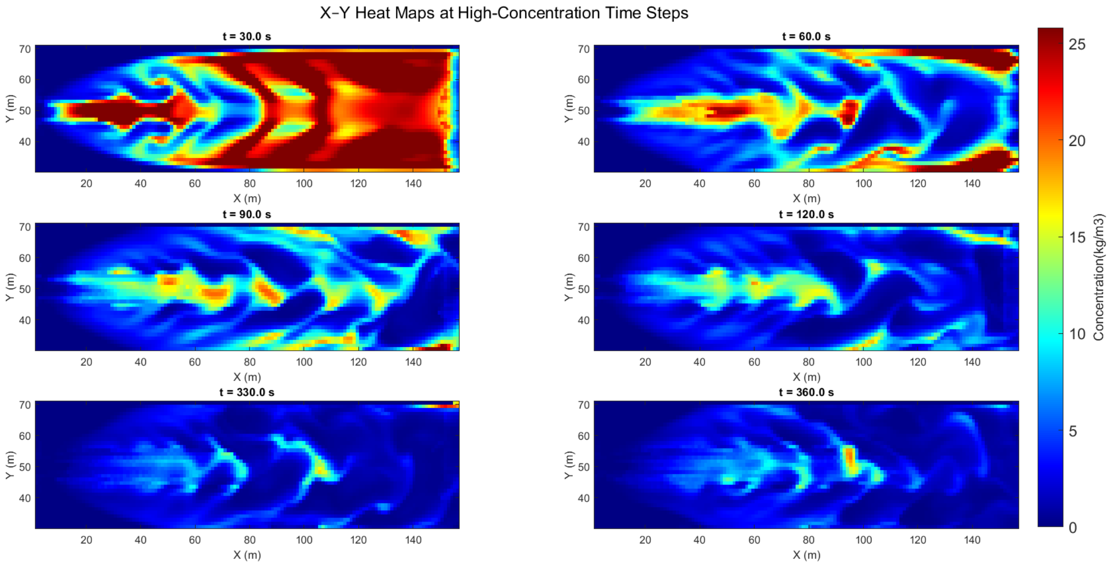

(b) LES – Fine Sand

Figure 16: High Concentration Heat Maps – Fine Sand

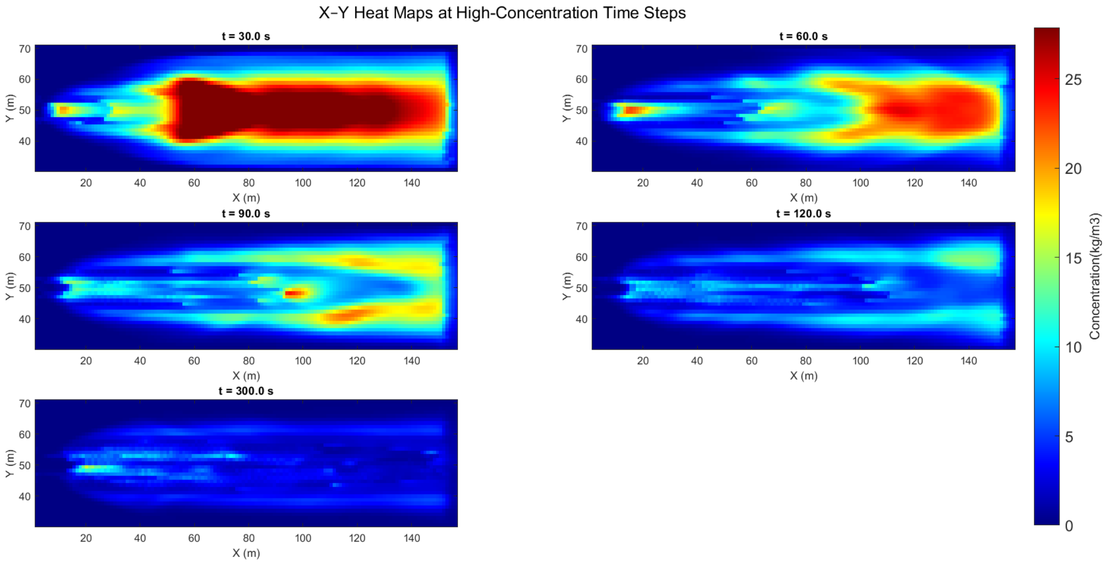

(a) RANS – Intermediate Sand

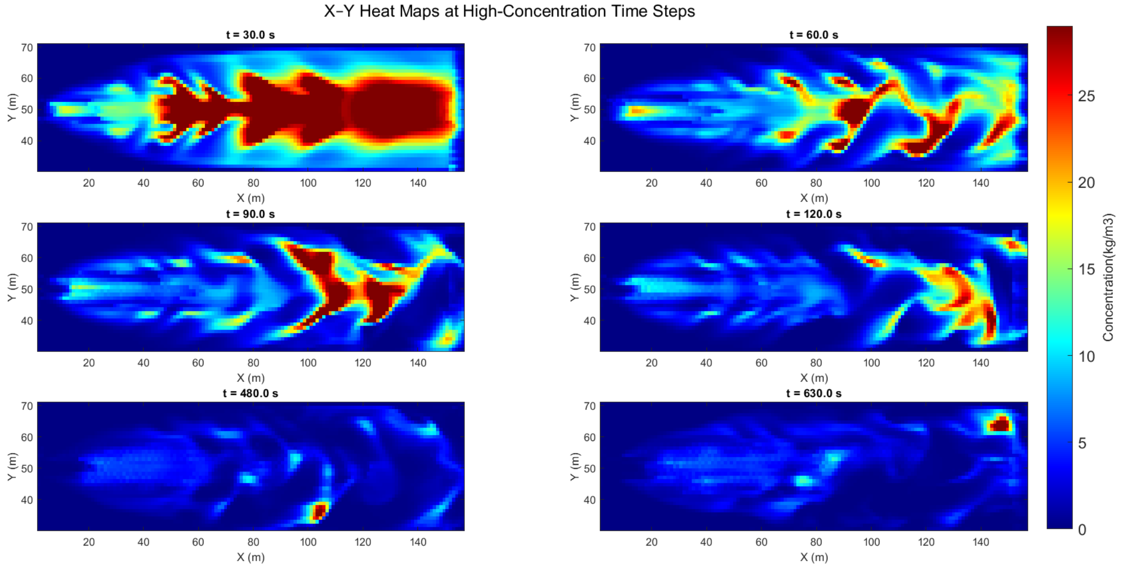

(b) LES – Intermediate Sand

Figure 17: High Concentration Heat Maps – Intermediate Sand

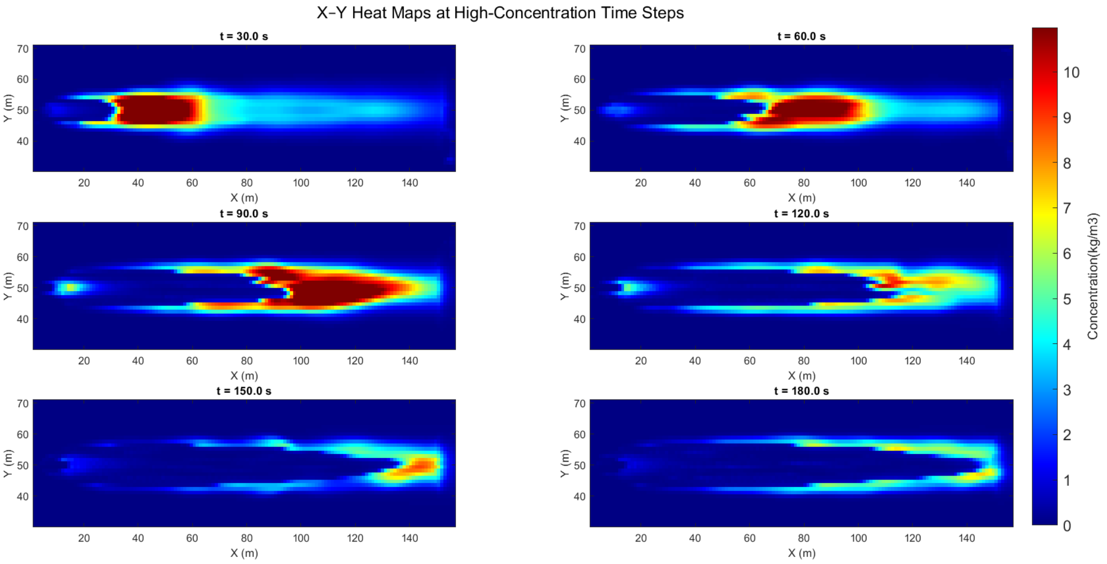

(a) RANS – Fine Gravel

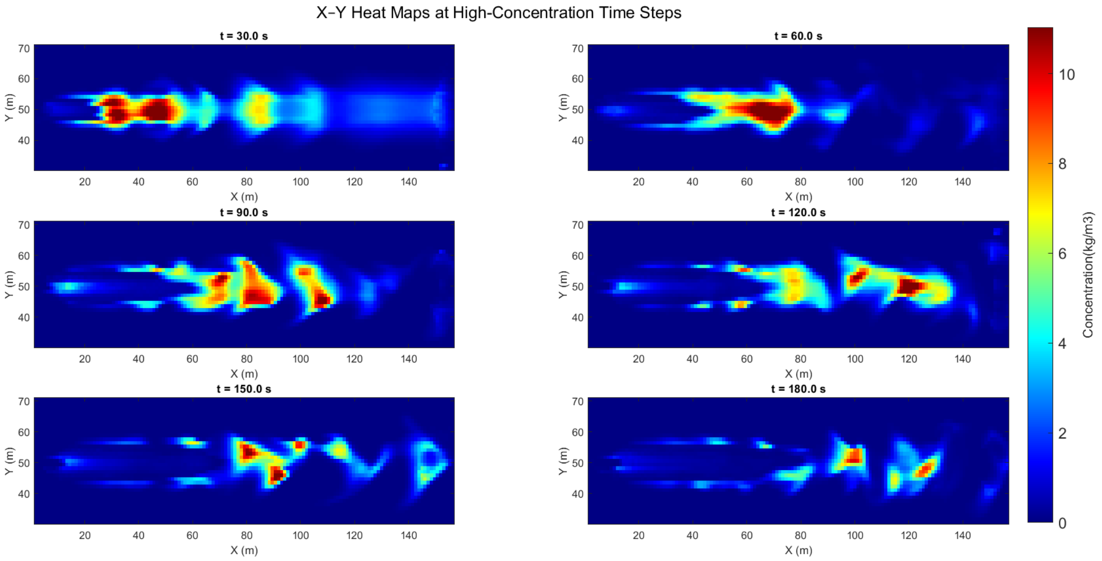

(b) LES – Fine Gravel

Figure 18: High Concentration Heat Maps – Fine Gravel

The centroid of the suspended sediment cloud was computed at each time step as a concentration-weighted mean position, defined as

$$\bar{x}(t) = \frac{\sum_i C_i(t)\, x_i}{\sum_i C_i(t)}, \qquad \bar{y}(t) = \frac{\sum_i C_i(t)\, y_i}{\sum_i C_i(t)} \tag{39}$$

where C_i is the suspended sediment concentration in cell i. Because this definition represents the center of mass of the entire suspended cloud rather than the location of the maximum concentration or the leading edge, the centroid remains confined to a relatively narrow downstream band (approximately 80–110 m) for all sediment classes throughout the simulation. This indicates that the bulk of the suspended sediment mass stays anchored in the jet impact and recirculation region, where repeated entrainment and mixing dominate, rather than undergoing a net downstream translation. The small fluctuations observed in the centroid trajectories reflect internal redistribution of suspended material within this region, while the lateral centroid position remains similarly stable, consistent with the confinement of the suspended cloud near the channel centreline. Overall, the centroid evolution characterizes the stability and internal variability of the suspended sediment body rather than its downstream transport.

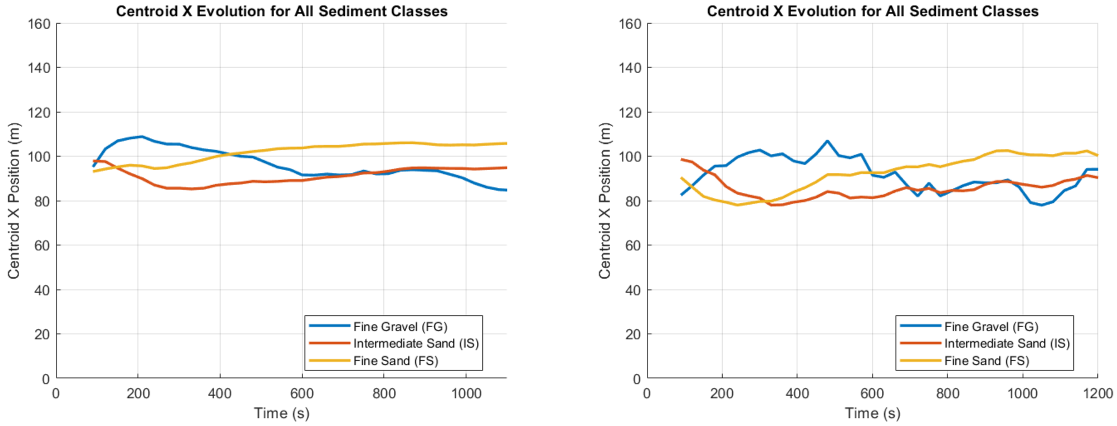

(a) RANS - Centroid X

(b) LES-Centroid X

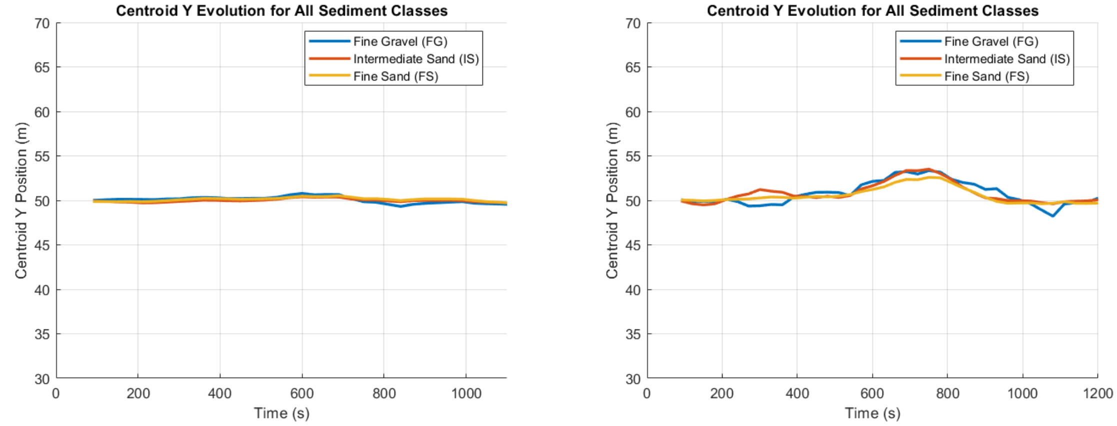

(c) RANS -Centroid Y

(d) LES-Centroid Y

Figure 19: Centroid Evolution in X and Y for All Sediment Classes

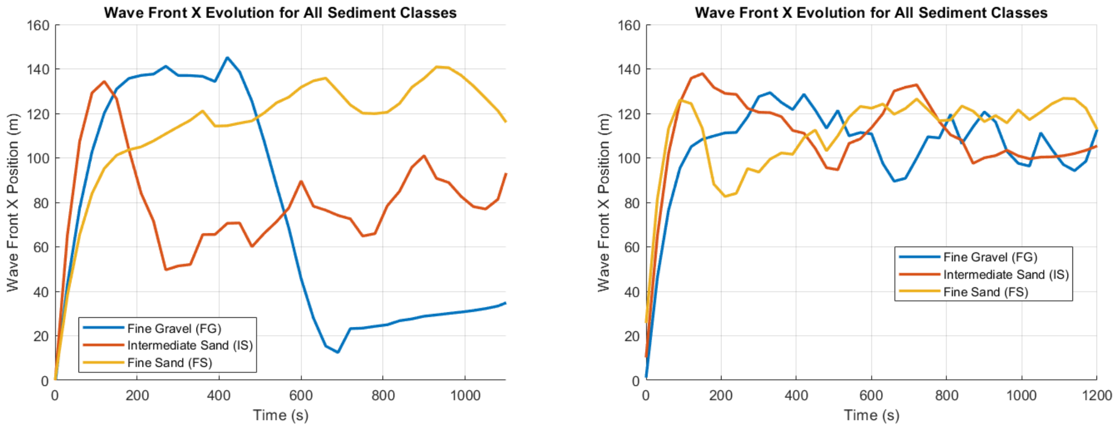

(a) RANS -Wavefront X (b) LES-Wavefront X

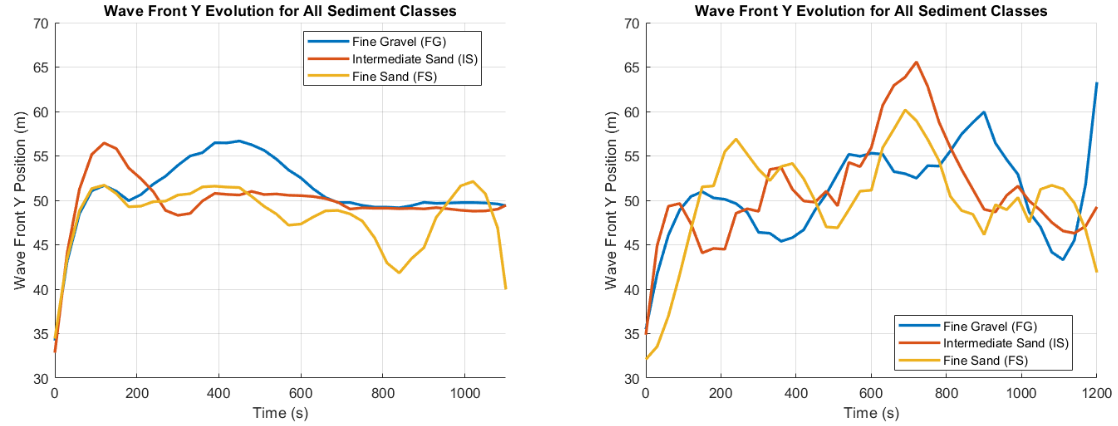

(c) RANS -Wavefront Y (d) LES-Wavefront Y

Figure 20: Wavefront Propagation in X and Y for All Sediment Classes

Sediment Class	Mean v_x (m/s)		RMS v_x (m/s)		Mean v_y (m/s)		RMS v_y (m/s)	
	RANS	LES	RANS	LES	RANS	LES	RANS	LES
F. Gravel (FG)	0.034	0.093	0.454	0.392	0.014	0.023	0.063	0.097
I. Sand (IS)	0.090	0.079	0.545	0.405	0.015	0.012	0.080	0.093
F. Sand (FS)	0.102	0.073	0.312	0.405	0.002	0.008	0.093	0.087

Table 8: Comparison of wavefront transport velocities for all sediment classes.

The sediment wavefront plots signify the evolution of the maximum concentration of suspended sediments in time and in main flow and lateral directions.The wavefront velocity comparison table (Tab. 8) highlights the difference between the two models in prediction sediment wavefront propagation in stream-wise and lateral directions across all three sediment classes.RANS predicts a smoother , monotonic advance of the wavefront downstream with increasing mean velocities for finer classes. LES on the other hand predicts slightly higher mean velocities for coarser classes, the reason being intermittent and unpredictable back and forth motion of the resolved eddies suspending the sediments.The RMS values in flow direction portray smaller variability for finer class by RANS while quite similar variability is shown for all three classes by LES, reflecting strong suspension intermittency under the resolved turbulent eddies. Both models show small lateral drift, but LES produces slightly larger values for FG and FS, consistent with eddy-driven lateral redistribution.LES generally shows higher lateral variability, especially for FG, indicating that even heavy particles experience short-duration lateral bursts under resolved eddies.

6 Conclusions

The primary objective of this study was to develop a robust numerical model capable of reproducing the hydrodynamic and sedimentation processes in the reservoirs of a pumped-storage hydropower(PSH) plant capable of operating in both turbining and pumping phases.A scaled physical model was developed in order to validate this numerical model and sets of experiments for the turbining case were performed. The numerical and experimental data in terms of time averaged and instantaneous velocity profiles, and shear stresses were extracted and compared to evaluate the fidelity of the numerical models(RANS and LES) in reproducing the experimental data. Furthermore, coupling of the RANS and the LES turbulence models with the sediment transport model was performed and the sediment dynamics and channel bed evolution results were compared to visualize the contrasts between these two models.

6.1 Key Findings

Mean Flow and Velocity Profiles Both RANS and LES models were able to reproduce the mean streamwise, vertical and horizontal velocity gradients at the intake/outlet section, 1-diameter and 2-diameter probe locations downstream.LES matched the experimental vertical and horizontal profiles and shear layers more closely, while RANS over-predicted the vertical velocity magnitudes.

Instantaneous Behaviour The experimental data showed oscillating streamwise velocity conditions at the intake , which neither LES or RANS were able to reproduce, the reason being that a constant velocity condition was specified in the numerical models. Although, LES was more efficient in reproducing the vertical and horizontal fluctuations in time at the 1-diameter and 2-diameter locations, producing broader PDFs that approached the experimental variability.

Near-Bed Shear The shear stresses and friction velocities obtained from the experimental model were higher, the reason being the difference in the bed roughness of the numerical and physical models. The shear stress development in time obtained from RANS and LES were comparably close and similar trends of increment and decrement were observed.

Sediment Transport In terms of sediment dynamics, LES produced a laterally broader and irregular suspension footprint and higher variability of suspended sediment concentrations while RANS yielded a narrower and axially aligned suspension and bed load movement. Centroid and Wavefront analyses showed that the suspended cloud remained largely confined to the main jet and recirculation regions for the RANS model, while the LES model produced strong intermittent lateral distributions.

RANS vs LES For shear and morphodynamics of the sediment bed, RANS provides a robust prediction of the mean fields and a smoother representation of shear stresses. The high shear stresses are concentrated along the jet axis, leading to smoother and more monotonic scour evolution from the simulations. LES on the other hand resolves the large eddies that spread the momentum laterally , creating localized shear patches. This leads to spatially heterogeneous sediment suspension and scour development.This is important when we want to assess localized erosion and short-term resuspension.

6.2 Limitations of the Numerical Model

Inflow Oscillations The numerical inflow conditions were steady while the experimental model intake section exhibited oscillating inflow velocity that was not implemented in the CFD, yet.

Bed Representation Mismatch The experimental bed of very coarse gravel produced macro-roughness and high friction velocities that were not captured by the homogenous packed bed and wall function approach in the numerical model.This is the main reason for the discrepancies in the shear stresses and friction velocities between the numerical and experimental models.

Limited SGS Model for LES The Sub-Grid Scale(SGS) model for LES simulations in the CFD code is limited to the Smagorinsky Model. Various other models such as Dynamic SGS model and the WALE model could improve the LES simulations.

Sediment Model The sediment transport model and the formulations used are not designed for cohesive fractions or for poorly sorted (i.e., well mixed) sediment sizes distribution. Calibration and code modifications might be further implemented in the future to account for specific cases.

7 Recommendations/Future Improvements

For Intake Transients Applying transient or oscillating inflow conditions in the numerical models, derived from the experimental results , will certainly improve the reproduction of the instantaneous fluctuations in the stream-wise direction of flow.This will be implemented following a thorough analysis of turbulent energy content and consequent optimization of inflow conditions in the experimental layout, still not finalized at the time of this work.

For Sediment Transport The numerical sediment data is yet to be compared and validated with the experimental sediment data, which is a future scope of this project.

For Improved Shear Agreement The shear stress and friction velocity results for the experimental model will conjugate better with the numerical data once a packed bed of matching sediment size is placed in the channel of the experimental model, which is a future scope of this project.

References

[1] International Energy Agency. *Pumped Storage Hydropower: Technology Brief.* 2022. URL: `https://www.iea.org/reports/pumped-storage-hydropower`.

[2] George W. Annandale et al. *Extending the Life of Reservoirs: Sustainable Sediment Management for Dams and Run-of-River Hydropower.* World Bank Publications, 2016. URL: `https://documents1.worldbank.org/curated/en/794841476187802040/pdf/108578-PUB-Box396309B-PUBLIC-PUBDATE9-23-16.pdf`.

[3] ANSYS Inc. *Theory of Standard, RNG, and Realizable k-epsilon Models.* Accessed via ANSYS Fluent Documentation. 2024. URL: `https://ansyshelp.ansys.com/public////////Views/Secured/corp/v242/en/flu_th/flu_th_sec_turb_all_ke.html`.

[4] María Bermúdez et al. "Hydraulic model study of the intake-outlet of a pumped-storage hydropower plant". In: *Engineering Applications of Computational Fluid Mechanics* 11.1 (2017), pp. 483–495. DOI: `10.1080/19942060.2017.1314869`.

[5] J.-L. Boillat et al. "Sediment management examples in Swiss Alpine reservoirs". In: *Proceedings of the International Workshop and Symposium on Reservoir Sedimentation Management.* Tokyo, Japan, 2000, pp. 26–27.

[6] H. Bormann et al. "Towards an indicator based framework analysing the suitability of existing dams for energy storage". In: *Water Resources Management* 28.6 (2014), pp. 1613–1630. DOI: `10.1007/s11269-014-0569-3`.

[7] Alberto Campisano et al. "Experimental and numerical analysis of the scouring effects of flushing waves on sediment deposits". In: *Journal of Hydrology* 299.1-2 (2004), pp. 324–334. DOI: `10.1016/j.jhydrol.2004.08.009`.

[8] European Commission Joint Research Centre. *Energy Storage Needs for a Decarbonised EU Energy System.* 2023. URL: `https://joint-research-centre.ec.europa.eu/publications/energy-storage-needs-decarbonised-eu-energy-system_en`.

[9] Sabine Chamoun et al. "Managing reservoir sedimentation by venting turbidity currents: A review". In: *International Journal of Sediment Research* 31.3 (2016), pp. 195–204. DOI: `10.1016/j.ijsrc.2016.06.001`.

[10] European Commission. *European Climate Law.* 2021. URL: `https://climate.ec.europa.eu/eu-action/european-green-deal/european-climate-law_en`.

[11] G. Constantinescu et al. "Large-eddy simulation of flow and turbulence structure in a channel with a vertical contraction". In: *Journal of Fluid Mechanics* 514 (2004), pp. 35–63.

[12] Flow Science, Inc. *FLOW-3D® Version 2025R1 User's Manual.* Computer software documentation. Santa Fe, NM, 2023. URL: `https://flow3d.com`.

[13] Massimo Germano et al. "A dynamic subgrid-scale eddy viscosity model". In: *Physics of Fluids A* 3.7 (1991), pp. 1760–1765. DOI: `10.1063/1.857955`.

[14] S.A. Hosseini et al. "Synchronous measurements of the velocity and concentration in low density turbidity currents using an Acoustic Doppler Velocimeter". In: *Flow Measurement and Instrumentation* 17.1 (2006), pp. 59–68. DOI: `10.1016/j.flowmeasinst.2005.05.002`.

[15] Kathleen Lyons et al. "Effects of wavelength on vortex structure and turbulence kinetic energy transfer of flow over undulated cylinders". In: *Theoretical and Computational Fluid Dynamics* 37 (2023), pp. 485–504. DOI: `10.1007/s00162-023-00633-4`.

[16] Dick R. Mastbergen et al. "Breaching in fine sands and the generation of sustained turbidity currents in submarine canyons". In: *Sedimentology* 50.4 (2003), pp. 625–637. DOI: `10.1046/j.1365-3091.2003.00554.x`.

[17] E. Meyer-Peter et al. "Formulas for Bed-Load Transport". In: *Proceedings of the 2nd Meeting of the International Association for Hydraulic Structures Research.* International Association for Hydraulic Structures Research. Stockholm, 1948, pp. 39–64.

[18] H. K. Moffatt et al. "A Brief Introduction to Vortex Dynamics and Turbulence". In: *Environmental Stratified Flows.* Ed. by R. Grimshaw. Singapore: World Scientific, 2011, pp. 1–30. DOI: `10.1142/9789814343411_0001`.

[19] F. Nicoud et al. "Subgrid-scale stress modelling based on the square of the velocity gradient tensor". In: *Flow, Turbulence and Combustion* 62.3 (1999), pp. 183–200. DOI: `10.1023/A:1009995426001`.

[20] Peter Nielsen. *Coastal Bottom Boundary Layers and Sediment Transport.* Singapore: World Scientific, 1992.

[21] S. Patil et al. "Comparison of Linear, Non-Linear and Generalized RNG-Based k-epsilon Models for Turbulent Diesel Engine Flows". In: *SAE Technical Paper* 2017-01-0561 (2017). DOI: `10.4271/2017-01-0561`.

[22] Leo C. van Rijn. "Sediment Transport, Part I: Bed Load Transport". In: *Journal of Hydraulic Engineering* 110.10 (1984), pp. 1431–1456. DOI: `10.1061/(ASCE)0733-9429(1984)110:10(1431)`.

[23] W. Rodi. *Turbulence Models and Their Application in Hydraulics.* IAHR Monograph, 1993.

[24] W. Rodi et al. In: *Large-Eddy Simulation in Hydraulics.* CRC Press / IAHR Monograph Series, 2013.

[25] W. Rodi et al. “Chapter 2: Basic Methodology of LES”. In: *Large-Eddy Simulation in Hydraulics.* CRC Press / IAHR Monograph Series, 2013.

[26] Wolfgang Rodi. *Turbulence Models and Their Application in Hydraulics: A State of the Art Review.* Presented by the IAHR Section on Fundamentals of Division II: Experimental and Mathematical Fluid Dynamics. Delft, The Netherlands: International Association for Hydraulic Research, 1980.

[27] Pierre Sagaut. *Large Eddy Simulation for Incompressible Flows.* 3rd ed. Springer, 2006. DOI: `10.1007/978-3-540-26344-9`.

[28] Joseph Smagorinsky. “General circulation experiments with the primitive equations”. In: *Monthly Weather Review* 91.3 (1963), pp. 99–164. DOI: `10.1175/1520-0493(1963)091<0099:GCEWTP>2.3.CO;2`.

[29] D. T. Souders et al. *Modeling Roughness Effects in Open Channel Flows.* Tech. rep. Technical Report. Flow Science, Inc., 2002. URL: `https://flow3d.com`.

[30] R. Soulsby. “Bedload Transport”. In: *Dynamics of Marine Sands.* Ed. by Richard Soulsby. London: Thomas Telford Publications, 1997. Chap. 9, pp. 145–170.

[31] T. Stoesser. “Large-eddy simulation in hydraulics: Quo vadis?” In: *Journal of Hydraulic Research* 48.6 (2010), pp. 666–677.

[32] Yasushi Takeda. *Ultrasonic Doppler Velocity Profiler for Fluid Flow.* Vol. 101. Fluid Mechanics and Its Applications. Springer, 2012.

[33] V. Yakhot et al. *Renormalization Group Analysis of Turbulence: RNG k-epsilon Model.* Tech. rep. 19920010431. NASA Technical Report, 1992. URL: `https://ntrs.nasa.gov/citations/19920010431`.

[34] Xudong Yang et al. “Downstream erosion and deposition dynamics of fine suspended sediment in dam flushing operations”. In: *Journal of Hydrology* 584 (2020), p. 124688. DOI: `10.1016/j.jhydrol.2020.124688`.